Earth and Space Science

Key Points:
- A multitiered observational network in California is evaluated during an extreme atmospheric river storm spanning 13–15 February 2019
- The network validates record precipitable water and detects mesoscale atmospheric processes driving flood, snowfall, and mass wasting events
- Diverse, high frequency observational networks are valuable investments to aid water resource management and natural hazard mitigation

Observations of an Extreme Atmospheric River Storm With a Diverse Sensor Network

B. J. Hatchett[1] , Q. Cao[2] , P. B. Dawson[3] , C. J. Ellis[4] , C. W. Hecht[4] , B. Kawzenuk[4] , J. T. Lancaster[5] , T. C. Osborne[4] , A. M. Wilson[4] , M. L. Anderson[6] , M. D. Dettinger[4] , J. F. Kalansky[4] , M. L. Kaplan[7] , D. P. Lettenmaier[2] , N. S. Oakley[1,4] , F. M. Ralph[4] , D. W. Reynolds[8] , A. B. White[9] , M. Sierks[4] , and E. Sumargo[4]

[1]Western Regional Climate Center, Desert Research Institute, Reno, NV, USA, [2]Department of Geography, University of California, Los Angeles, CA, USA, [3]U.S. Geological Survey, Moffett Field, Menlo Park, CA, USA, [4]Center for Western Weather and Water Extremes, Scripps Institution of Oceanography, La Jolla, CA, USA, [5]California Geological Survey, Sacramento, CA, USA, [6]California Department of Water Resources, Sacramento, CA, USA, [7]Applied Meteorology Program, Embry-Riddle Aeronautical University, Prescott, AZ, USA, [8]Department of Atmospheric and Oceanic Sciences, University of Colorado, Boulder, CO, USA, [9]NOAA/Earth System Research Laboratory/Physical Sciences Division, Boulder, CO, USA

Abstract Observational networks enhance real-time situational awareness for emergency and water resource management during extreme weather events. We present examples of how a diverse, multitiered observational network in California provided insights into hydrometeorological processes and impacts during a 3-day atmospheric river storm centered on 14 February 2019. This network, which has been developed over the past two decades, aims to improve understanding and mitigation of effects from extreme storms influencing water resources and natural hazards. We combine atmospheric reanalysis output and additional observations to show how the network allows: (1) the validation of record cool season precipitable water observations over southern California; (2) the identification of phenomena that produce natural hazards and present difficulties for short-term weather forecast models, such as extreme precipitation amounts and snow level variability; (3) the use of soil moisture data to improve hydrologic model forecast skill in northern California's Russian River basin; and (4) the combination of meteorological data with seismic observations to identify when a large avalanche occurred on Mount Shasta. This case study highlights the value of investments in diverse observational assets and the importance of continued support and synthesis of these networks to characterize climatological context and advance understanding of processes modulating extreme weather.

1. Introduction

California's complex terrain, biogeographical diversity, proximity to the data-sparse North Pacific Ocean, and large population and economy provide an environment both dependent upon and highly susceptible to weather and climate extremes (Cayan et al., 2016; Lundquist & Cayan, 2007). These include extreme precipitation events, flooding, land-surface mass wasting, multiyear droughts and pluvials, heat waves, and wildfires (Dettinger et al., 2011; Lamjiri et al., 2017; Oakley, Cannon, et al., 2018; Oakley, Lancaster, et al., 2018; Ralph et al., 2006; Swain, 2015). Many of these extremes are projected to worsen or become more impactful in a warming climate (Bedsworth et al., 2018).

Water resources in California rely on precipitation and snowpack resulting in large part from landfalling atmospheric rivers (ARs) associated with cool season midlatitude cyclones (Figure 1a; Dettinger et al., 2011; Rutz et al., 2014). While often beneficial, the hydrometeorological impacts associated with ARs also bring significant emergency management challenges and expenses (Corringham et al., 2019; Ralph et al., 2019). Managing and reducing these challenges and costs requires accurate understanding of what, where, and when various impacts are occurring. However, weather models initialized over data-poor locations such as oceans (e.g., Nardi et al., 2018) provide inadequate information. This creates a need for networks of readily available, high resolution, and diverse observations. Such networks facilitate tracking, evaluation, and anticipation of storm-related impacts and impact-triggering thresholds necessary for natural hazard early warning and achievement of water resource management objectives (Moore et al., 2015; Oakley et al., 2017; Oakley, Lancaster, et al., 2018; Ralph et al., 2014; Sterle et al., 2019; Uccellini & Ten Hoeve, 2019; White et al., 2013).
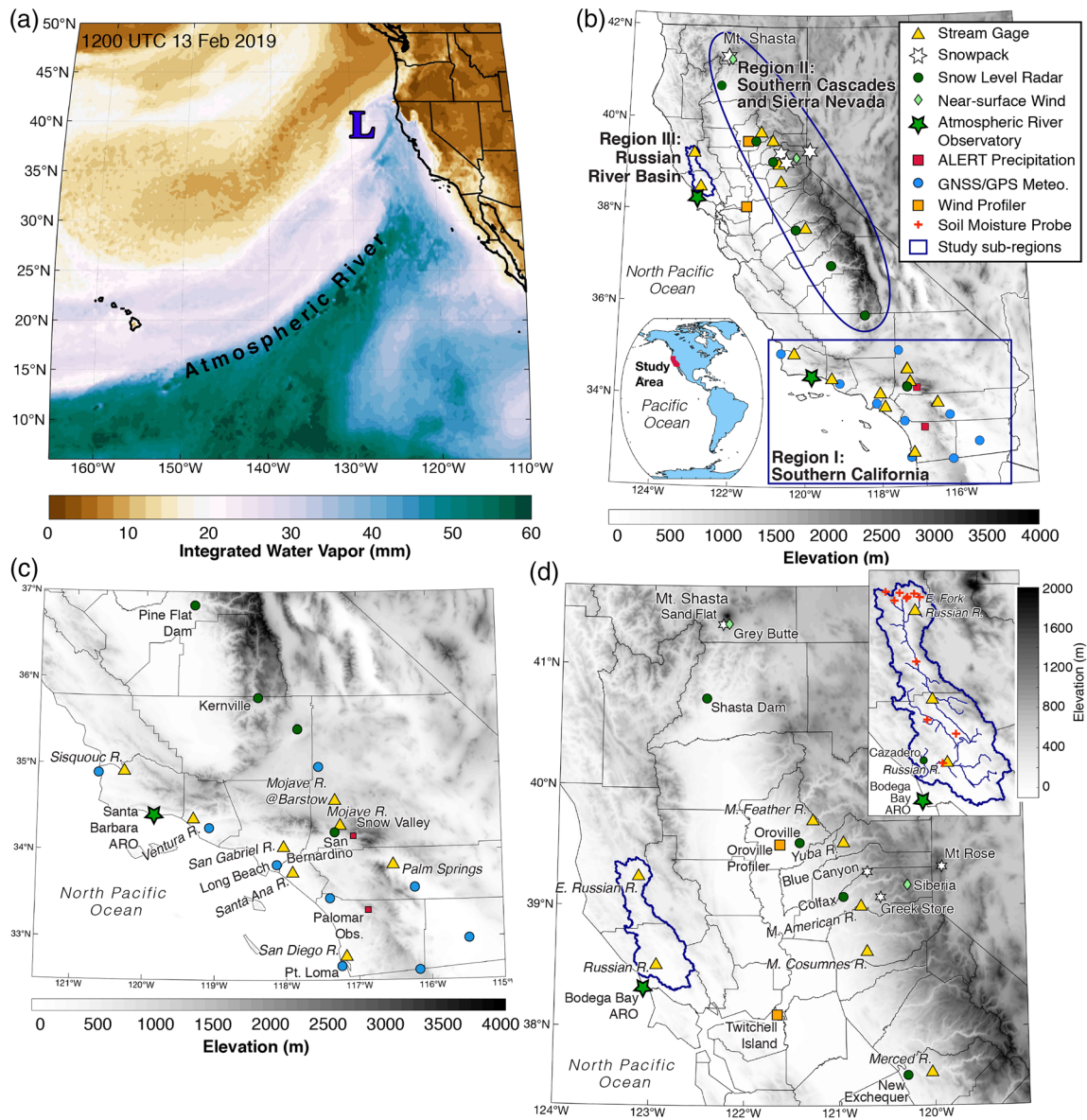
Figure 1. The Valentine's Day landfalling atmospheric river and select observations used in the study. (a) Satellite-derived integrated water vapor (IWV; mm) at 1200 UTC 13 February 2019 showing the surface cyclone (labeled with a blue "L") and the moisture plume (labeled as "atmospheric river"). (b) Map of specific observations from California's multitiered observation network and focus regions of the study. Topography and observations for (c) Region I (southern California) and (d) Regions II (southern Cascades and Sierra Nevada; section 5) and III (Russian River watershed (inset); section 6).

To accommodate these data needs in California, a multitiered network of observations has been implemented and expanded since the early 2000s (Figure 1b; Ray & White, 2019; White et al., 2013). This network evolved from the goal of understanding extreme events in California to a broader vision aimed at observing the mountainous western United States (Ralph et al., 2014). It includes sensors with different levels of technology, novelty, and costs (see Table 1 for specific components used in the present study). It is supported by a wide variety of agencies at the federal, state, county, and local levels as well as private groups. Some components of the network, such as snow level radars and AR observatories (AROs), have been installed as part of the jointly-supported National Oceanic and Atmospheric Administration (NOAA)/California Department of Water Resources Hydrometeorology Testbed (HMT) and are tracked by the NOAA Observing System Council (White et al., 2013). Others, like the Global Navigation Satellite Systems/Global Positioning System (GNSS/GPS) network, leverage sensors with differing primary goals to extend precipitable water observations over land (e.g., Bevis et al., 1992). Lower tiers of the network include proven, cost-effective

Table 1
Observational Data Used

| Network	Details	Additional information
Hydrometeorology Testbed (HMT) West Legacy Observing Network	A California Department of Water Resources network installed and operated by NOAA's Oceanic and Atmospheric Research (OAR) Physical Sciences Division (PSD). Instruments include: precipitation gauges and disdrometers, various wind and temperature profiling radars, GPS, stream level loggers, soil moisture probes, snow pillows, and more.	https://hmt.noaa.gov/ White et al. (2013)
Snow Level Radars	NOAA Earth Systems Research Laboratory and California Department of Water Resources joint radar network allowing for novel measurements of bright band (melting layer) heights.	Johnston et al. (2017)
Atmospheric River Observatories (AROs)	Evolved from HMT-West, a small network with a combination of three to four instruments including radar wind profilers, GPS IWV sensors, standard surface meteorology stations, and in some cases snow level radar.	White et al. (2009)
GNSS/GPS	A global network originally developed for positioning, navigation, and time transfer that now has many more uses including atmospheric/climate studies due to their ability to measure zenith tropospheric delay as a function of temperature, pressure, and water vapor.	https://www.suominet.ucar.edu/index.html https://hmt.noaa.gov/
Atmospheric River Reconnaissance	Observations by aircraft dropsondes (flight paths shown in Figure 4a) and buoys in the Northeast Pacific Ocean intended to improve existing forecasts of ARs while supporting research to improve weather models, data assimilation methods, and reconnaissance targeting methods.	http://cw3e.ucsd.edu/arrecon_overview/ Ralph et al. (2020)
Radiosondes	Radiosonde observations are made throughout the country by the National Weather Service and compiled and made available by the University of Wyoming. Several other research groups, such as CW3E at Scripps, also record radionsonde data.	http://weather.uwyo.edu/upperair/sounding.html
Automated Local Evaluation in Real-Time (ALERT)	Wireless sensor network providing local agencies with real-time flood warnings, but can also monitor wind, temperature, humidity barometric pressure, soil moisture, fuel moisture, and more.	https://www.alertsystems.org/index.php/about-us
USGS Water Data	Nationwide network of USGS sites with real-time or recent and historic stream gage data.	https://waterdata.usgs.gov/nwis/sw
Palomar Observatory National Weather Service Cooperative Observer (COOP) Network	Long-term, daily observations of temperature, precipitation, snowfall, and occasionally evaporation or soil temperature. Forms the United States component of the Global Historical Climatology Network-Daily.	https://www.ncdc.noaa.gov/data-access/land-based-station-data/land-based-datasets/cooperative-observer-network-coop
MIMIC-TPW2 IWV observations	An experimental global product of satellite-derived total precipitable water using morphological compositing of microwave integrated retrieval system (Liu & Weng, 2005) retrievals from operational microwave frequency observations.	http://tropic.ssec.wisc.edu/real-time/mtpw2/ Wimmers and Velden (2010)
gridMET	A daily gridded data set of high-spatial resolution (6 km) surface meteorological variables covering the contiguous United States.	http://www.climatologylab.org/gridmet.html Abatzoglou (2013)
USGS Northern California Earthquake Data Center	USGS program, including comprehensive monitoring of earthquakes, that is part of the National Earthquake Hazards Reduction Program (NEHRP).	https://ncedc.org/
Sub-daily meteorological observations	Sub-daily observations supported by various agencies and available from the California Data Exchange Center (CDEC) and MesoWest.	mesowest.utah.edu/ http://cdec.water.ca.gov/
NOAA California-Nevada River Forecast Center (CNRFC) freezing level forecasts	Twice-daily forecasts of freezing level height produced using forecaster input and a blend of operational models (e.g., GFS) using a "top down" approach to find the elevation of the mean areal freezing level (0°C) isotherm. 150–200 m are subtracted from this elevation to account for the time it takes a falling hydrometeor to melt. During flood events, forecasts may be issued every 6 hr.	https://www.cnrfc.noaa.gov/about/products_summary.php https://www.cnrfc.noaa.gov/about/hydromet_forecasting.php
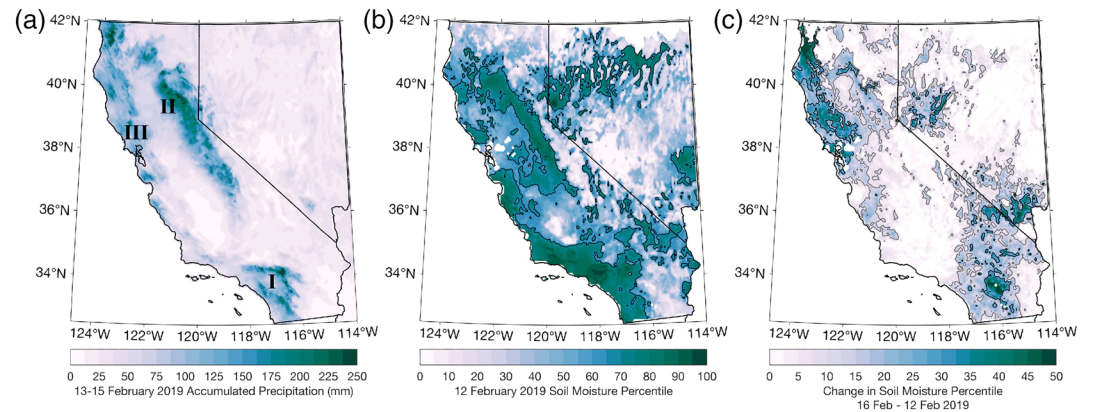
Figure 2. Event precipitation and root zone soil moisture conditions prior to and following the storm. (a) Accumulated 13–15 February 2019 precipitation from the 4 km gridMET product (Abatzoglou, 2013). (b) Antecedent soil moisture percentiles on 12 February 2019 estimated from the Variable Infiltration Capacity model (Liang et al., 1994). Black contours enclose percentiles within the top tercile (>66%). (c) Change in soil moisture percentile between 12 February and 16 February 2019. The gray and black contours enclose changes exceeding 10% and 25%, respectively.

technology augmenting existing standard weather stations such as soil moisture, snow water equivalent, and snow depth. Higher tiers, such as snow level radar, targeted dropsondes from offshore aircraft-based reconnaissance flights, and gap-filling radar, are more novel and costlier (Cifelli et al., 2018; Cordeira et al., 2017; Johnston et al., 2017; White et al., 2013).

Here we demonstrate how select data from this network, in conjunction with additional available atmospheric and hydrologic modeling and observational data, provide a posteriori insight into statewide processes and impacts resulting from an extreme winter AR event, the "Valentine's Day Storm" spanning 13–15 February 2019 (Figure 1). This storm satisfied the duration and integrated water vapor (IWV) transport criteria to be categorized as an AR 5 (extreme or exceptional) using the AR scale of Ralph et al. (2019). Storms of this magnitude reach northern California approximately once every 4 years (Ralph et al., 2019). Three-day accumulated precipitation exceeded 200 mm (Figure 2a) and increased soil moisture percentiles by as much as 25 points (Figures 2b–2c). The observed rainfall totals exceeding 200 mm during the storm satisfy the first level of the R-CAT scale, which documents extreme multiday precipitation (R-CAT 1; Ralph & Dettinger, 2012). Such events have return periods ranging from approximately 2 to 10 years in the mountains of California (Lamjiri et al., 2020).

Impacts from this storm were widespread and varied. Documented impacts included riverine and alluvial fan flash flooding, evacuations from burned areas, avalanches, landslides, and disruptions to transportation and commerce from road closures. We focus on three different regions of California (Figure 1b) to highlight the value of monitoring networks in documenting an extreme hydrometeorological event. The regions include southern California (region I), the southern Cascades and Sierra Nevada (region II), and the Russian River watershed (region III). We begin with a synoptic meteorological analysis (section 3). Observations and impacts from each region are presented as separate subcase studies (sections 4–6) intending to highlight the added value the network provides with respect to understanding storm processes and impacts in particular locations. We end with discussion regarding how observational networks support the achievement of broader water resource management and natural hazard mitigation goals amidst a changing climate in a geographically diverse state (sections 7–8).

2. Observational Data and Model Products Used

Our primary focus is on ground-based sensors with real-time data availability (Ralph et al., 2014). To provide a holistic, comprehensive look at the event statewide as well as to supplement interpretations of ground-based sensors, we also utilized additional observations (Table 1). These observations include radiosondes; dropsondes from flights over the North Pacific Ocean; ALERT tipping bucket precipitation gauges; and data from four U. S. Geological Survey (USGS) Northern California Seismic Network seismometers

installed on Mount Shasta (Northern California Earthquake Data Center (NCEDC), 2014). The seismic instruments are used to constrain the timing of a large avalanche event on Mount Shasta (southern Cascades) during the storm.

In addition to observations, we leverage operational and reanalysis-based atmospheric model output to support interpretations made using observational data and provide broader context. We incorporate 0.5° × 0.625° horizontal resolution, 3-hourly output from the Modern-Era Retrospective Reanalysis Version 2 (MERRA-2; Gelaro et al., 2017) to estimate return intervals of integrated vapor transport (IVT) and IWV. These return intervals are calculated using meteorological winters (December–February) spanning 1980–2019. IVT is a useful metric to include because it shows promise in advancing forecast lead time (Lavers et al., 2016). We use potential vorticity on the 330 K surface from the higher resolution (compared to MERRA-2) hourly 0.25° Global Forecast System final analysis (GFS; NOAA Environmental Modeling Center, 2003) to diagnose Rossby wave breaking (RWB), a common precursor to extreme midlatitude weather events (e.g., Hu et al., 2017; Rondanelli et al., 2019), via the overturning of potential vorticity surfaces (Abatzoglou & Magnusdottir, 2006). The GFS output spans 2015–present, therefore we could not use it to calculate return intervals. However, its greater spatial resolution improved our ability to diagnose potential vorticity gradients and wave breaking.

Semi-distributed hydrologic modeling is employed to characterize antecedent land surface conditions and their response to storm precipitation statewide. Daily, 7 km horizontal resolution, soil moisture percentiles corresponding to the soil root zone depth (1.4–2.53 m) are estimated using the Variable Infiltration Capacity model (VIC; Liang et al., 1994). These percentiles give a climatological perspective on soil root zone moisture conditions but do not explicitly provide soil saturation. Last, we provide a modeling experiment using the Distributed Hydrology Soil Vegetation Model (DHSVM; Wigmosta et al., 1994) in the flood-prone Russian River watershed, where new approaches to reservoir management are being developed (Talbot et al., 2019). This experiment highlights the value of soil moisture information for improving model initialization and flood forecasting.

3. Large-Scale Atmospheric Conditions

The Valentine's Day storm exhibited many common ingredients characterizing extreme winter season storms at planetary to synoptic scales of motion. At 0600 UTC 13 February 2019 large-scale atmospheric conditions were characterized by amplified planetary waves and active cyclonic and anticyclonic RWB (Abatzoglou & Magnusdottir, 2006; Thorncroft et al., 1993) over the western and eastern margins of the North Pacific Basin, respectively (Figure 3a; supporting information Figure S1). The cyclonic RWB in the western Pacific induces cyclogenesis and promotes the formation of a downstream ridge near the dateline (180°W) and a persistent trough over the eastern Pacific (Moore et al., 2019). AR conditions (IVT exceeding 250 kg m^{-1} s^{-1}; Ralph et al., 2019) with strong poleward and eastward transport of moisture were observed along the eastern flanks of the high potential vorticity air (Figure 3a), consistent with RWB and diabatic forcing of cyclogenesis (Hu et al., 2017).

Equatorward of the planetary-scale anticyclonic RWB, a zonally extended coupled polar and subtropical trans-Pacific jet stream exceeding 40 m s^{-1} existed with the divergent left jet exit region positioned over northern-central California. A surface cyclone was located offshore of the northern California coast under the cyclonic shear side of the jet stream. The zonally extended middle-upper tropospheric flow undercutting an amplified ridge with axis near the dateline is a favorable scenario for heavy precipitation in California (Underwood et al., 2009) with high snow levels (Hatchett, Daudert, et al., 2017). The upper level jet, anticyclonic RWB in the polar stream, and subtropical moisture connection promoted elevated atmospheric moisture and moisture transport over southern California (Payne & Magnusdottir, 2014; Figures 3b–3c). The southwesterly orientation of this moisture transport enhanced upslope water vapor flux and helped produce heavy orographic precipitation in mountains oriented perpendicular to onshore flow (e.g., Ralph et al., 2013).

Two plumes of strong water vapor transport are evident in the IVT field (Figure 4a). Both displayed modeled IVT values exceeding 1,000 kg m^{-1} s^{-1} but very different IWV values (Figure 4b). The northern plume 1 is wind-dominated, inferred from its lower values of IWV (30–40 mm) compared to the southern plume 2, which had offshore IWV in exceedance of 50 mm. The northern plume made landfall in northern
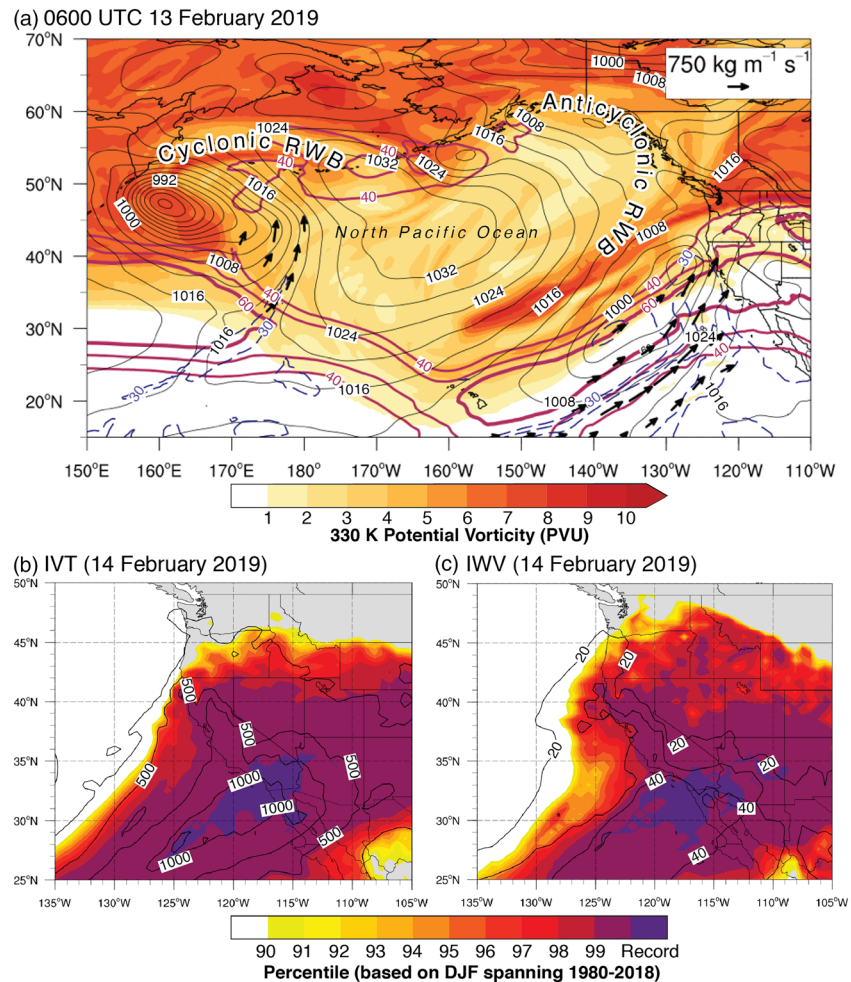
Figure 3. Large-scale atmospheric conditions over the North Pacific Ocean and western North America at 0600 UTC 13 February 2019 from the 0.25° Global Forecast System final analysis. Shown in (a) are 330 K Isentropic Potential Vorticity (PVU; filled contours), 200 hPa wind speed (solid maroon contour; m s^{-1}), sea-level pressure (solid black contour; hPa), integrated water vapor (IWV; dashed blue contour; mm), integrated water vapor transport (IVT) vector (plotted according to reference vector in upper right; kg m^{-1} s^{-1}); (b) percentiles of 14 February 2019 IVT based upon 1980–2018 MERRA-2 winter (December–February; DJF) climatology (filled contours) and IVT values (black contours; kg m^{-1} s^{-1}); (c) as in (b) but for IWV (contours have units of mm).

California while the southern plume made landfall in southern California. A vertical cross section from aircraft observations transecting the AR core and perpendicular to the direction of mean moisture transport (Figure 4c) further highlights the differing IWV and moisture transport characteristics of the IVT plumes. Both plumes demonstrated elevated moisture fluxes deep into the midtroposphere (850–700 hPa; Figures 4c and S2). The moisture in the southern plume extended above 500 hPa (Figure 4c) and was transported poleward from the tropics by a northeastward-moving Kona Low (Morrison & Businger, 2001).

4. Record Southern California Atmospheric Moisture

A multitude of impacts occurred throughout Southern California (Figure 5) as a result of favorable large-scale atmospheric conditions for heavy precipitation. Record moisture availability and above-average soil moisture facilitated many precipitation-related impacts. The GNSS/GPS network observed IWV exceeding 30 mm throughout Southern California (Figure 5), with Point Loma observing a peak value of 46 mm at 1715 UTC (Figure 6a). The IWV observation from the 1200 UTC 14 February
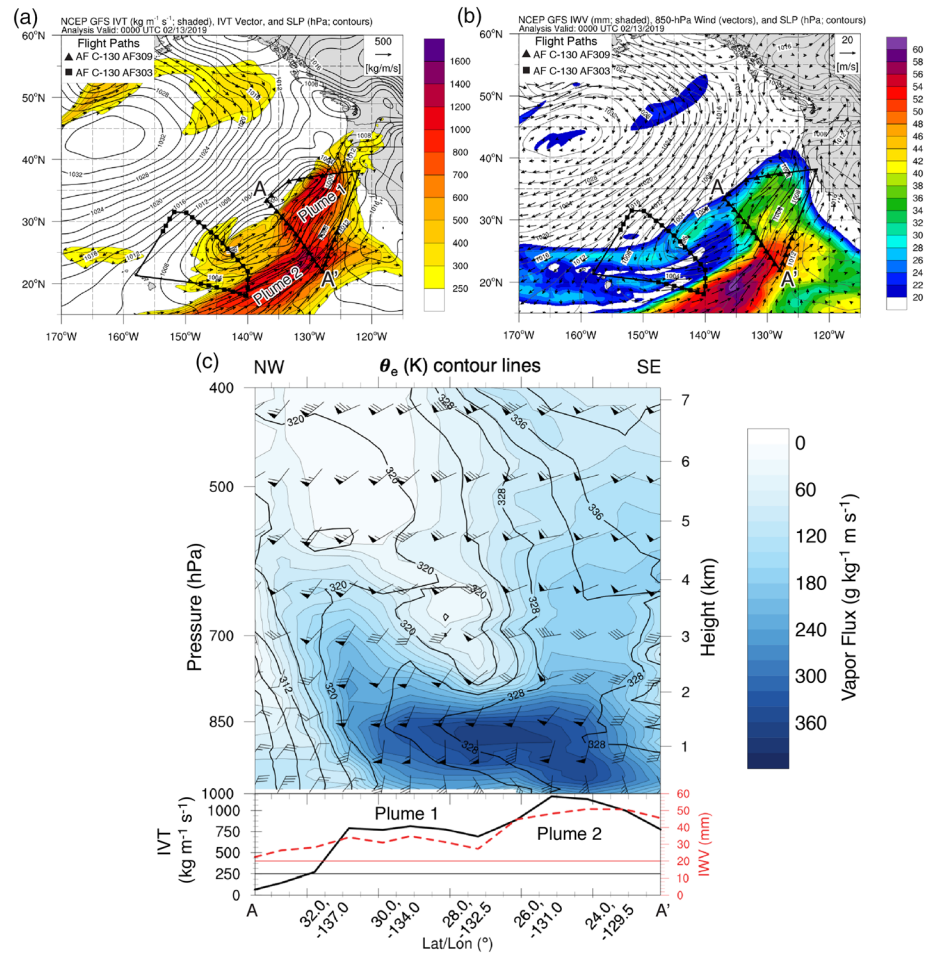
Figure 4. Model simulations and aircraft observations of the atmospheric river. (a) Global Forecast System simulated sea level pressure (open contours; hPa), integrated vapor transport (IVT; filled contours; kg m^{-1} s^{-1}), and IVT vectors for 0000 UTC 13 February 2019. Aircraft flight paths are shown by black lines with symbols. (b) Global Forecast System simulated sea level pressure (open contours; hPa), integrated water vapor (IWV; filled contours; mm), and 850 hPa wind vectors (m s^{-1}) for 0000 UTC 13 February 2019. The black lines in (a) and (b) show flight paths and the triangles denote dropsonde release locations from the aircraft. (c) Dropsonde-derived vertical cross section of equivalent potential temperature (θ_e), wind barbs (m s^{-1}), and water vapor flux across the two IVT plumes identified in (a). The lower panel of (c) shows cross sectional IVT (black line) and IWV (dashed red line).

2019 radiosonde launched from Miramar, CA (Figure 6a), set a cool season (October–April) record at 42.7 mm. This value was supported by a 1500 UTC radiosonde launched at the SIO pier in La Jolla that observed 45.4 mm (Figures 6a and S3). Offshore dropsonde-derived IWV observations exceeded 50 mm (Figure 4c), consistent with GNSS/GPS and satellite observations (Figure 2a). The large-scale dynamics (Figure 3a) and extreme IVT and IWV (Figures 3b–3c) promoted upslope water vapor flux (Neiman et al., 2009; Figures 6b–6d), creating an environment conducive to orographically enhanced extreme rainfall (Ralph et al., 2013).

To characterize land surface conditions before and after the Valentine's Day storm, we examined the soil moisture conditions using the University of California Los Angeles drought monitor (available at http://www.hydro.ucla.edu/SurfaceWaterGroup/forecast/monitor_ca/index.html; Mao et al., 2015; Xiao et al., 2017). Soil moisture in the drought monitor is reconstructed by the VIC model following Bohn et al. (2013). Precipitation fell on soils nearing saturation throughout Southern California due to wetter-than-normal conditions resulting from previous AR landfalls, most notably a strong (AR 4) storm that made landfall near Point Conception on 2 February 2019. Prior to the Valentine's Day event, soils were in the upper quartile of modeled soil moisture percentiles relative to the 1920–2010 climatology of the VIC
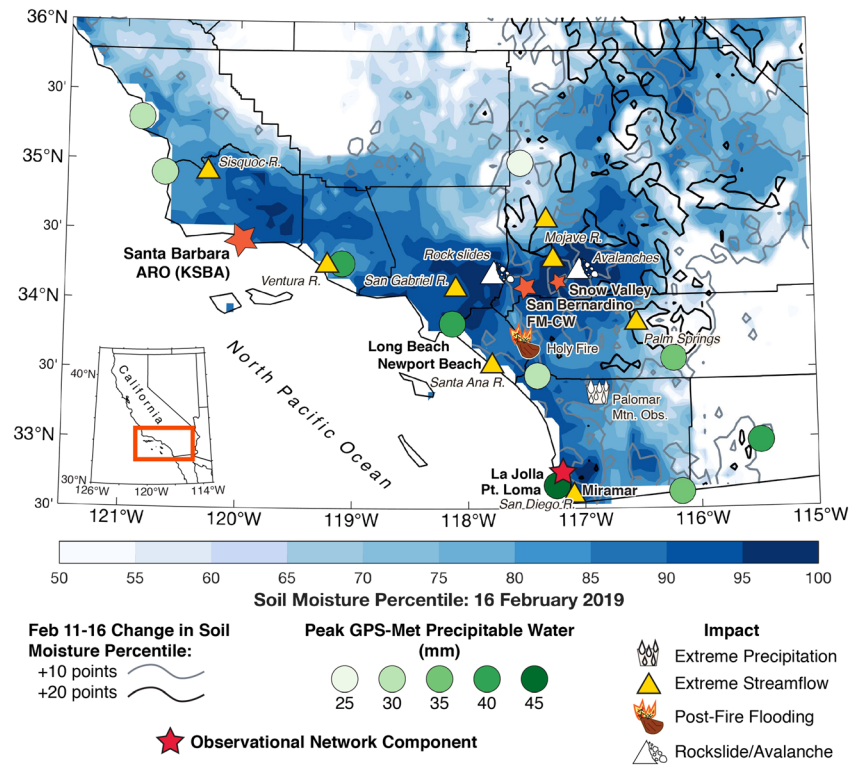
Figure 5. VIC-estimated soil moisture percentiles in Southern California on 16 February 2019 (filled contours) and soil moisture percentile changes between 12 and 16 February 2019 (open contours). Colored dots indicate peak event integrated water vapor (IWV; mm) at GNSS/GPS sensors. Icons denote observed impacts and red stars indicate observation locations.

model (Figures 2b and 5). These conditions favored runoff generation in both the uplands and lowlands. Ephemeral washes in the Palm Springs Desert observed the greatest flows since records began in 1987 (Figure 5). A debris flow in Chino Canyon damaged the Palm Springs Aerial Tramway (Desert Sun, 2019). Peak flows along inland-draining rivers with longer periods of record were notable. Many ocean-draining and urbanized rivers also achieved flow rates that exceeded the top 3% of flow rates on record (yellow triangles in Figure 5). For example, the Mojave River reached the top 0.2% of flows since observations began in 1930. Rainfall-triggered mass movements were not confined to southern California; landslides were also documented in the San Francisco Bay area (Collins & Corbett, 2019) and in the western foothills of the Sierra Nevada.

Rainfall was extreme in measures of intensity and total accumulations. The National Weather Service Cooperative Observer rain gauge at Palomar Observatory (elevation 1,702 m), in northern San Diego County, measured 256 mm of rainfall in 24 hr. This was the highest 24-hr total since record keeping began in 1943. A colocated, sub-hourly ALERT gauge observed a similar total with periods of intense rainfall (Figure 6c) likely corresponding to the development of stronger convective cells. Many mountain regions in southern California observed rain rates exceeding U. S. Geological Survey general guidance for 15-min intensity-duration thresholds for triggering post-fire debris flows (ranging between 12.5 and 21.8 mm hr^{-1}; Cannon et al., 2008; Staley et al., 2017). Hyperconcentrated flows and alluvial fan flash floods were observed in recently burned regions such as the Holy Fire (Figure 5) where 12-hr precipitation totals exceeded the 200-year return interval causing widespread flash flood impacts. The extreme precipitation at Snow Valley combined with snow levels exceeding 3 km contributed to full-path avalanches in the San Gorgonio Mountains (Figures 5–6). Numerous landslides in the San Gabriel Mountains occurred, with one causing a 30-km segment of the Angeles Crest Highway to be closed for 8 months (Burgess et al., 2019; Figure 5).
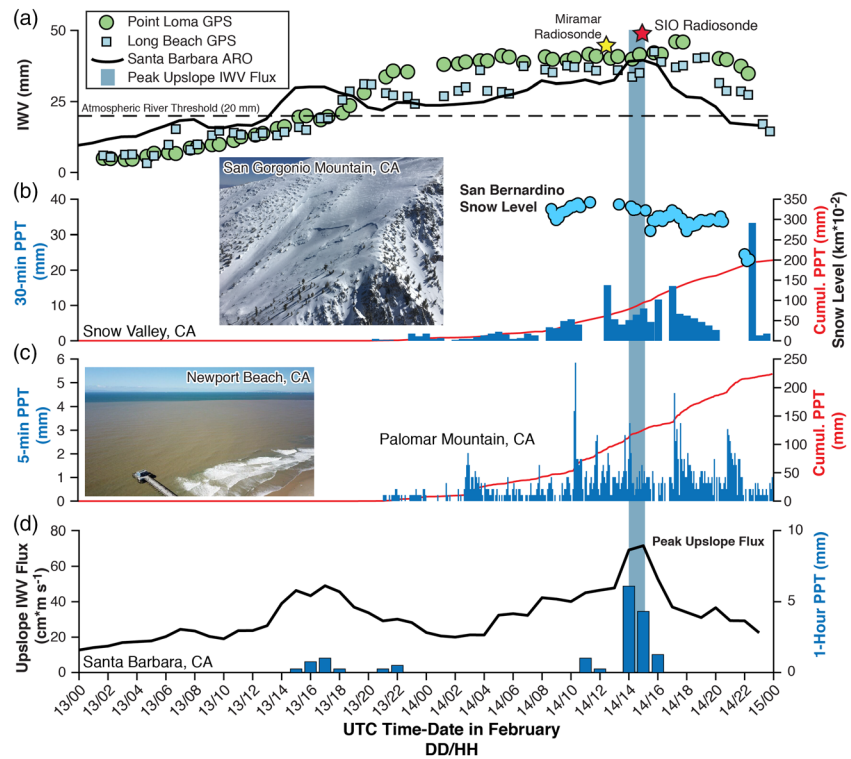
Figure 6. Southern California observations during 13–15 February 2019. (a) Time series of GNSS/GPS-derived IWV (mm) at Point Loma, Long Beach, and the Santa Barbara Atmospheric River Observatory (ARO) and radiosondes from Miramar and the Scripps Institution of Oceanography. (b) Sub-hourly precipitation at Snow Valley ALERT gauge (blue bars; mm) and cumulative precipitation (red line; mm) with San Bernardino snow levels (blue dots; km*10^{-2}). Image of the Mt. San Gorgonio avalanches (photo credit: Mike Nobriga via the So Cal Avalanche Center, http://www. socalsnow.org/avalanche-report-2-19-19-san-gorgonio.html). (c) As in (b) but for Palomar Mountain ALERT gauge. Newport Beach photograph provided by Royce Hurtain. (d) Upslope integrated water vapor flux (cm*m s^{-1}), calculated by multiplying IWV and the upslope wind speed 1 km above the surface, obtained from the Santa Barbara ARO (Neiman et al., 2009). The shaded blue bar denotes the approximate time period of the peak upslope water vapor flux.

5. Observations and Impacts in California's Sierra Nevada and Southern Cascades

5.1. Snow Level Variability

Abrupt changes in snow level often accompany winter storms with varying impacts on hydrology, recreation, and transportation (White et al., 2019). Rises in snow level correspond to increases in streamflow as the advection of warm, moist air facilitates snowmelt and a growing fraction of the watershed receives rainfall (Hatchett et al., 2016, 2018; White et al., 2010). Snow level oscillations exceeding 1,000 m and exceeding durations of 30 min were observed in the Sierra Nevada, with the ultimate snow level rise progressing from south to north (Figure 7). The varied timing and duration of these oscillations indicates mesoscale variability in snow level conditions throughout the Sierra Nevada (Minder et al., 2011; Minder & Kingsmill, 2013). Operational weather models have difficulty simulating variable situations, as demonstrated in the suite of California-Nevada River Forecast Center (CNRFC) freezing level forecasts (Figures 7c–7d). These difficulties arise from microphysical processes that may not be well-resolved in operational models due to parameterization schemes and grid spacing (Minder & Kingsmill, 2013). Melting level forecast errors were also found to increase both with lead time and increasing rain-snow transition elevation (Henn et al., 2020). Although some CNRFC ensemble members correctly approximate snow level rise timing and magnitude (Figures 7a–7b), many estimate the snow level to be more than 1,000 m lower than the level observed by the radar. This bias may lead to errors in streamflow forecasts in snow-dominated watersheds (e.g., White et al., 2010).
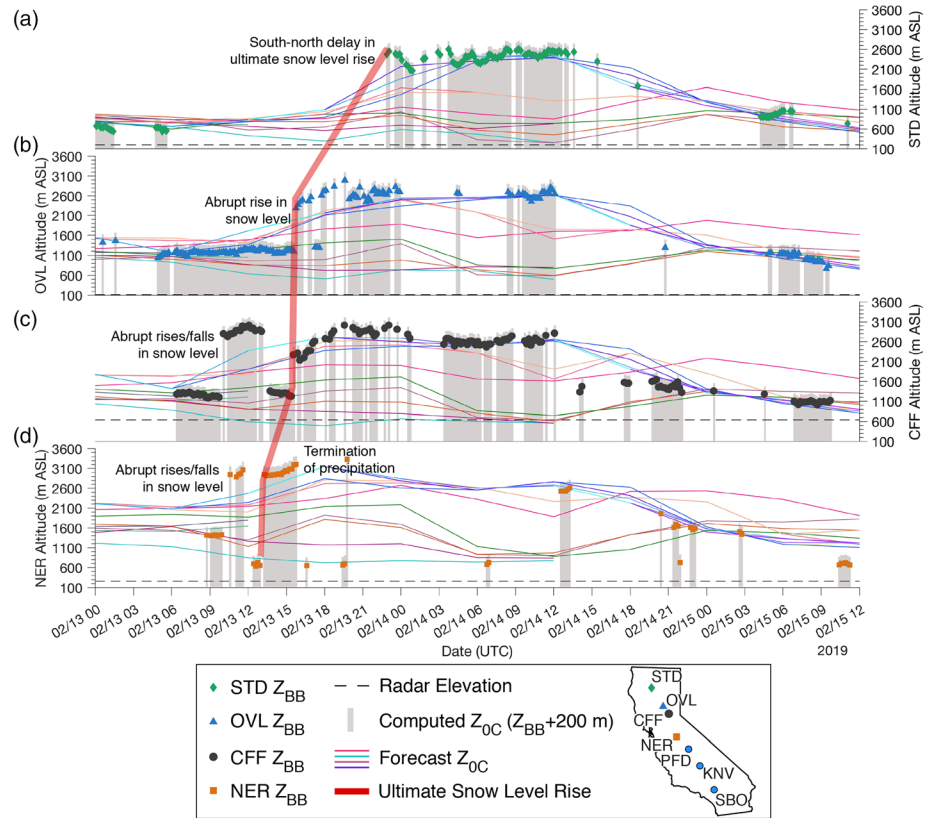
Figure 7. Snow level oscillations and California-Nevada River Forecast Center (CNRFC) freezing level forecasts from north to south in Region II. Time series of snow levels at (a) Shasta Dam (STD), (b) Oroville (OVL), (c) Colfax (CFF), and (d) New Exchequer (NER) snow level radar brightband heights (m; shown as symbols for each site), CNRFC freezing level forecasts (colored lines; m), and freezing level based on radar brightband heights (m; computed by adding 200 m to each brightband value to account for the typical vertical distance between freezing level and snow level; Lundquist et al., 2008; White et al., 2010) for the period spanning 0000 UTC 13 February to 1200 UTC 15 February 2019. Each radar location's elevation is shown as a dashed black line. The inset map shows locations of all snow level radar observations used in the study.

Figure 8. Ten-minute snow level percentiles for seven snow level radars in California spanning the period 2000 UTC 12 February 2019 to 0000 UTC 15 February 2019. Ordered from north to south, stations names are Shasta Dam (STD), Oroville (OVL), Colfax (CFF), New Exchequer (NER), Pine Flat Dam (PFD), Kernville (KNV), and San Bernardino (SBO).

Expressing snow levels as percentiles provides another perspective of the magnitude of snow level variability during this event (Figure 8). Percentiles are calculated using 10 min data for the December–February period over the respective periods of record for each radar (>5 years). Consistent with near-freezing temperatures at Shasta Dam (Figure 9a), low snow levels (bottom tenth percentile) were observed before rising into the upper fifteenth percentile. The absence of a brightband (Figure 9a) despite precipitation observations (Figure 9b) resulted from the brightband elevation being below the radar site. In the northern and central Sierra Nevada, snow level oscillations occurred between the upper and lower quartiles at Oroville, Colfax, and New Exchequer (Figure 8). This created varying snowpack responses with elevation (Figures 9e–9f). The lower elevation Blue Canyon and Greek Store snow pillows showed snow depth decreases throughout the event whereas depth increased at Mount Rose, a higher elevation station (Figure 9e). Snow water equivalent increased at all stations except Blue Canyon (Figure 9f). The increased streamflow following the snow level oscillation was realized at the Middle Forks of the American and Cosumnes River (Figure 9g) at approximately 1600 UTC 13 February 2019 and 0000 UTC 14 February 2019, respectively.
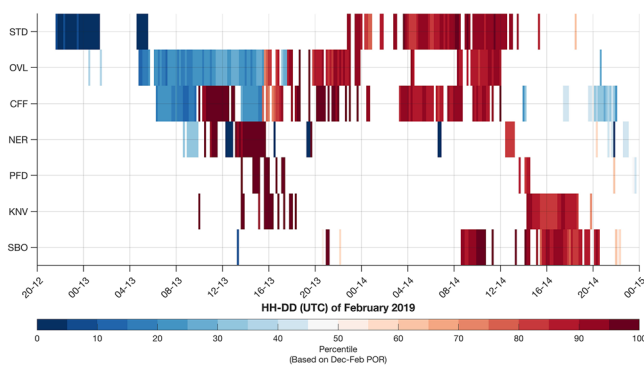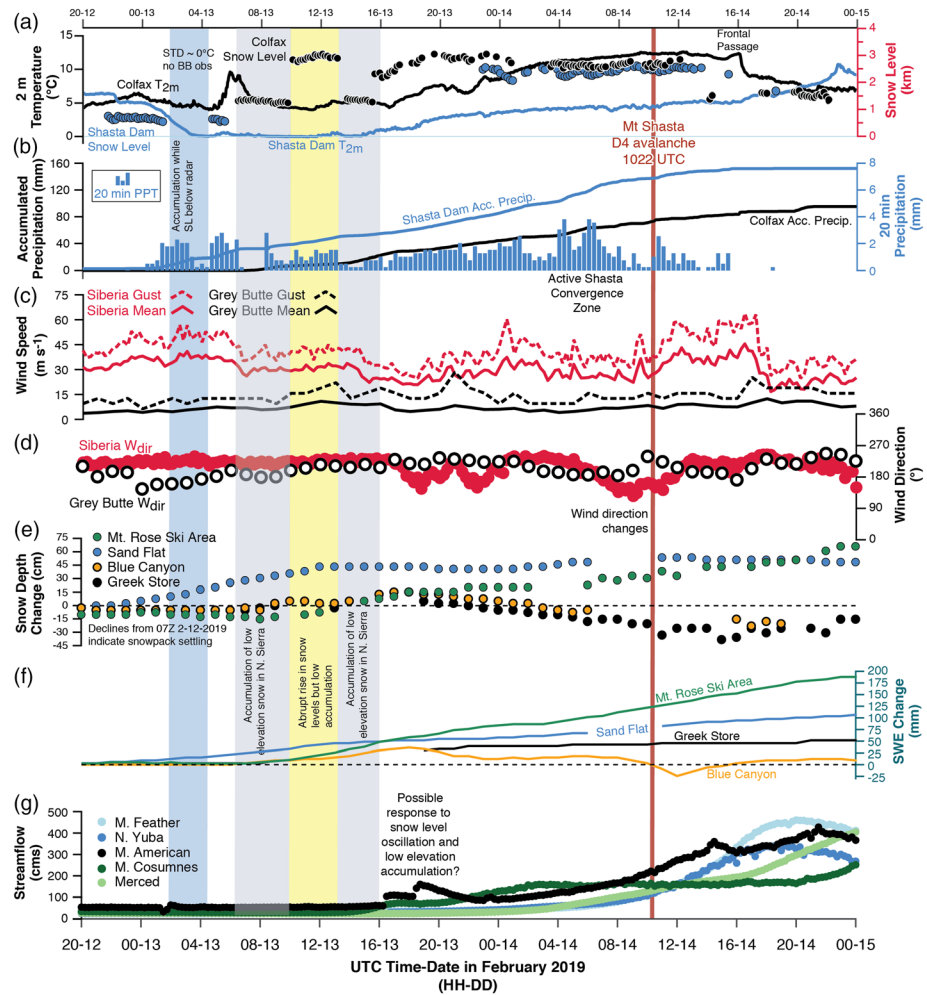
Figure 9. Time series of southern Cascades/northern Sierra Nevada observations from surface meteorological stations for the period spanning 2000 UTC 12 February 2019 to 0000 UTC 15 February 2019. (a) Near-surface (2 m) temperature (left axis; solid lines; °C) and snow level (right axis; colored dots; km) with black lines and dots corresponding to the Colfax station and blue lines and dots corresponding to the Mt. Shasta Dam station. (b) Accumulated precipitation (left y axis; mm) and 20 min precipitation (blue bars; right y axis; mm), (c) wind speed and gust (both in m s^{-1}), and (d) direction (°) along the Sierra Nevada Crest (Siberia Ridge; in red) and south of Mt. Shasta (Gray Butte; black), (e) snow depth change (cm), (f) snow water equivalent (SWE) change (mm), and (g) streamflow (cms). The vertical red line corresponds to the timing of the Avalanche Gulch avalanche observation diagnosed from the seismic network on Mt. Shasta (section 5.3). Station locations are shown in Figures 1d and 10.

Snow level observations in the southern Sierra Nevada showed different responses than those in the north. Sporadic observations between 1300 and 1800 UTC 13 February 2019 at Pine Flat Dam and Kernville (Figure 8) demonstrate the transition region between the northern and southern IVT plumes (Figures 4a–4b). We interpret these observations as representing the equatorward boundary of the initial wave of precipitation associated with the northern moisture plume. The southern moisture plume is characterized by high (top tenth percentile) snow levels throughout its duration at Kernville and San Bernardino, consistent with 0°C elevations exceeding 4,000 m observed by offshore dropsonde measurements (Figure S2). Brightband observations at San Bernardino began approximately 6 hr before Kernville and no brightband was observed further north until 2000 UTC 14 February 2019 when cold frontal passage occurred (Figure 9a). This suggests the southern plume only impacted Southern California, and is consistent with the termination of brightband observations at New Exchequer at 1600 UTC 13 February (Figure 8).

5.2. Snow Impacts on Mountain Transportation

Many of California's main transport routes pass through mountainous regions and are susceptible to closures or delays that impact economic activity. During 13 February 2019, snow levels were among the lowest 5% of hourly observations during the past decade (2010–2019; Figure 8) at the Shasta Dam snow level radar site (elevation 202 m) before the brightband elevation fell below the station elevation (Figure 9a). Over 20 cm of snowfall was recorded in Redding, California (172 m), an uncommon occurrence in this area. Mount Shasta City (1,000 m) recorded 60 cm of snowfall (Mount Shasta Avalanche Center, 2019). This heavy low elevation snowfall slowed interstate commerce along Interstate 5 from the normal average of ~61,000 vehicles day^{-1} to ~24,000 vehicles (California Department of Transportation (Caltrans), 2019). Traffic restrictions along Interstate 80 over the Sierra Nevada, a major east-west highway (average annual daily traffic of 35,000), began at 1800 UTC 13 February 2019 with a full closure from 0200 UTC 14 February 2019 to 0100 UTC 16 February 2019. Using average annual daily traffic volumes for each road with truck percentages of 12%, and a delay cost of $0.46 min^{-1} for trucks and $0.24 min^{-1} for cars (California Department of Transportation (Caltrans), 2019), we estimate net commerce loss to be on the order of $21 M during the Valentine's Day storm for these two major highways. This value represents a minimum estimate as delay costs for other impacted roads, such as Highway 50, and costs of repairs to damaged roads (e.g., Angeles Crest Highway; section 4) are not included.

5.3. Mount Shasta Avalanche Timing and Triggering

Here we show how geologic observations can be leveraged to provide further insight into impacts from this storm. At approximately 1800 UTC 14 February 2019, evidence of a very large (R4/D4.5; Figures 10a–10b) avalanche with a 5 km path length (Figure 10c) was discovered in the Avalanche Gulch on the southwestern flank of Mount Shasta. Avalanche Gulch is a glacially sculpted canyon composed of steep sidewalls with numerous start zones at elevations between 3,000 and 4,000 m. Avalanche paths converge in the canyon bottom and terminate in gently sloping forested terrain 1,000 m below. Depositional debris from this avalanche was approximately 10–20 m deep with 10 m tall flanks (Figure 10b). Avalanches of this magnitude on Mount Shasta are relatively rare, occurring on decadal scales (Hansen & Underwood, 2012).

The addition of over 80 mm of snow water equivalent (Figure 9f) is consistent with snowpack instability caused by continuous loading of new snow during AR events (Hatchett, Burak, et al., 2017). The Mount Shasta Avalanche Center advisory for 13 February was "high," indicating naturally triggered large avalanches are likely. Synoptic conditions (section 3) were consistent with those previously linked to large Mt. Shasta avalanches (Hansen & Underwood, 2012).

In the absence of human observations, the local seismic network (Figures 10d–10f) can be used to constrain the avalanche timing. The network recorded a high-energy spindle-like signal emerging from the background noise at 1022 UTC 14 February 2019 that lasted for ~2 min, followed by ~20 min of increased seismic energy. The waveforms observed at each station are broadband with frequencies ranging from 1–15 Hz and are dominated by energy between 2 and 5 Hz. These characteristics have been tied to avalanche activity by Kishimura and Izumi (1997). The signal duration (~2 min) and avalanche path length (5 km) yield an avalanche velocity of 42 m s^{-1}, consistent with dry or mixed slab avalanches (Vilajosana et al., 2007). The two increases in energy within the wavetrain (Figure 10d) suggest distinct pulses in the avalanche process. Potential cultural origins of the seismic signal, notably train operations, were ruled out via spectral analysis and a second, smaller avalanche possibly occurred at 1740 UTC 14 February 2019.

Constraining the avalanche timing provides insight into potential triggering mechanisms. The avalanche occurred many hours after snow levels rose (Figure 9a), however the "upside-down" nature of the snowpack (more dense snow deposited atop less dense snow) inferred from lower snow levels followed by high snow levels (section 5.1) favors snowpack instability. Regional winds from the ground-based observations (Figure 9c) and the Oroville and Twitchell Island wind profilers (Figure S4) indicate accelerations in low-level (2–4 km; ~850–700 hPa) winds to 25 m s^{-1} at 0400 UTC 14 February with a turning of upper level winds to a more southeasterly direction (Figure 9d). These winds are reminiscent of the Sierra Nevada barrier jet that enhances northward moisture flux in the Central Valley (Neiman et al., 2013; Parish, 1982),
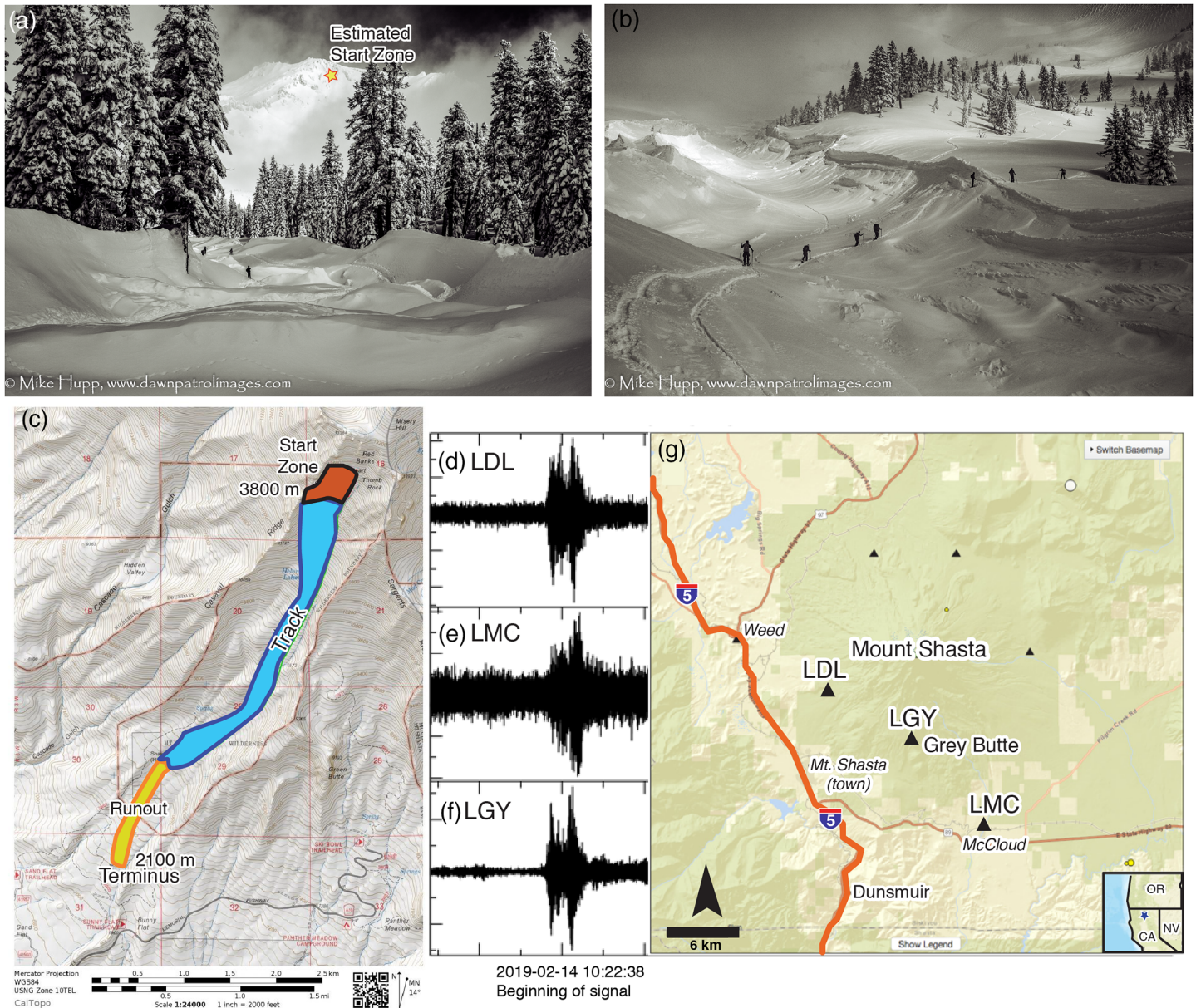
Figure 10. The Mt. Shasta avalanche. (a–b) Images of the avalanche from the runout zone (skiers for scale; images courtesy of Mike Hupp). (c) Avalanche path map provided by the Mount Shasta Avalanche Center. (d–f) Seismic signals from three seismometers located on the southwestern flank of Mount Shasta (times in UTC). (g) Location map of the seismic stations (triangles) and the Gray Butte weather station (colocated with LGY).

increases precipitation in the northern Sierra Nevada and southern Cascades (Ralph et al., 2016), and helps establish the Shasta County Convergence Zone (Roberts, 2019; Figure 9b). Although the avalanche initiated on a southerly aspect normally scoured by prevailing southwesterly winds, deposition on this slope may have resulted from interactions of southerly winds aloft (Figures 9d and S4) with Mt. Shasta. The low-level westerly flow at the Gray Butte (Figure 9d) station on the south flank of Mt. Shasta, despite southerly flow aloft (Figure S4), suggests airflow interactions with the mountain. Snow levels did not rise above 3 km (Figure 9a), rendering it unlikely that free-water introduction (Prowse & Owens, 1984) played a role in avalanche initiation in the start zone of Avalanche Gulch. In contrast, the San Gorgonio avalanches (section 4) appeared to have occurred much closer in elevation (within 500 m) to the snow/rain transition elevation (Figure 6).
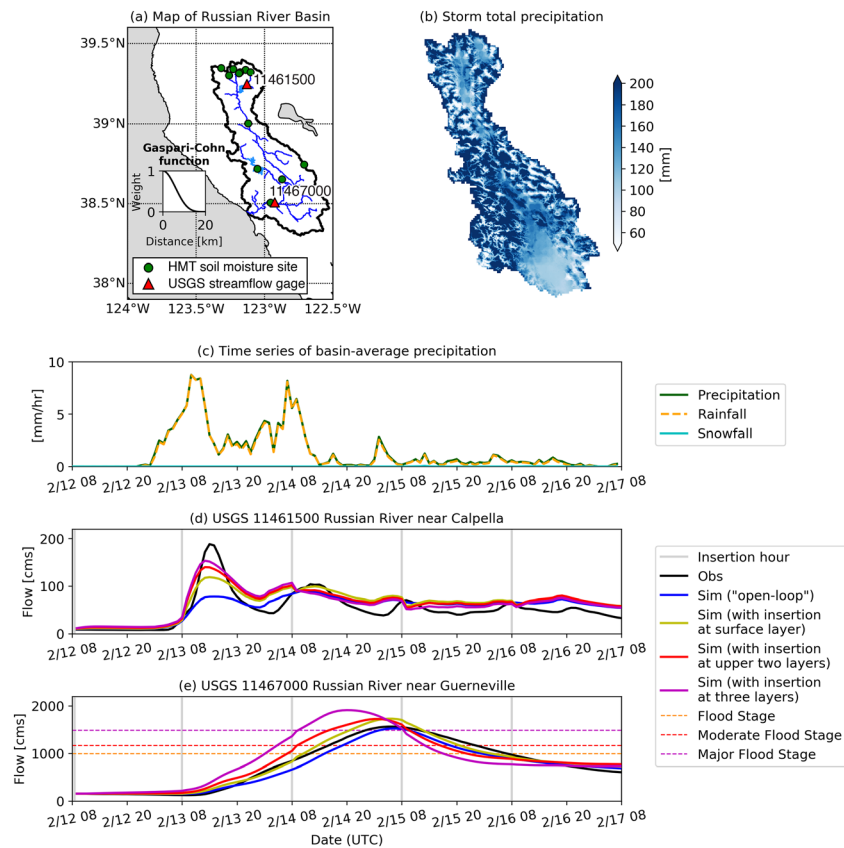
Figure 11. Hydrologic modeling results from the Russian River watershed. (a) Map of the Russian River basin, with locations of USGS stream gages and Hydrometeorology Testbed (HMT) soil moisture observation sites shown. (b) Map of storm total precipitation. (c) Time series of hourly basin-average total precipitation and total precipitation as rain and snow. Observed and simulated hourly streamflow time series during the storm at upstream USGS gages (d) 11461500 and (e) 11467000. Gage 11467000 is impacted by reservoir operations at Lake Mendocino and Lake Sonoma, the effect of which has been removed in the observed streamflow time series shown.

6. Soil Moisture Improves Russian River Streamflow Forecasts

6.1. Hydrologic Modeling Approach

To provide a direct example of how observations from the Valentine's Day storm can be used for hydrologic modeling in a flood-prone watershed, we conducted an experiment applying the Distributed Hydrology Soil Vegetation Model (DHSVM; Wigmosta et al., 1994) to the Russian River watershed in northern California (Region III in Figure 1b; see also Figure 1d inset). This watershed was among the first to have AR-flood relationships identified in California (Ralph et al., 2006). As a result, AROs and dense hydrologic monitoring instrumentation (Sumargo et al., 2020; White et al., 2013) were installed to inform flood management. In recent years, this basin has served as a proof-of-concept watershed for testing the viability of forecast-informed reservoir operations aimed at improving flood control and water supply operations (Talbot et al., 2019).

The goal of the Russian River modeling experiment is to examine the potential use of soil moisture sensors in model initialization and flood forecasting. We used the same model implementation as in Cao et al. (2019), in which calibration was performed for the period 2005–2014 at multiple stream gages. We used 12 HMT soil moisture sites (Figure 11a) with at least 3 years of data and included measurements during the Valentine's Day storm. The DHSVM as applied to the Russian River basin has three root zone soil layers with depths at 10, 35, and 75 cm. We extended the 1/32° horizontal resolution gridded, hourly precipitation data used as input to the model and developed by Cao et al. (2019) through the Valentine's Day event (Figures 11b–11c). We note that due to its low elevation (0–1,200 m; 90% of the watershed is below

630 m), the Russian River basin is not a snow-dominated watershed. Thus, we do not expect streamflow responses to be related to snow level variability (e.g., section 5.1) as in snow-dominated catchments in the Sierra Nevada (White et al., 2010). Virtually no precipitation during this event fell as snow over the Russian River basin (Figure 11c).

We used the HMT measurements at depths of 10, 15, and 50 cm (the deepest measurement depth at most sites) as the corresponding model layers. In order to reconcile the soil moisture range difference in observations and the model, we converted both to hourly soil moisture percentiles relative to extended winter (November–March spanning 2017–2019) for each layer. We updated the model throughout the storm at a daily interval at midnight local time (0700 UTC) using a simple direct insertion approach for all soil layers. The observed soil moisture percentiles were interpolated over the basin using a Gaspari-Cohn function (Gaspari & Cohn, 1999) with a radius of 20 km where the weight decreased as the distance between an observation site and a target model grid cell increased (Figure 11a). We then interpolated the percentiles back to model values to update the soil moisture initialization state. We examined the effects of updating for the surface soil layer only, the upper two layers, and all three layers. We then explored the effects of this procedure at two USGS streamflow gages, the unimpaired upstream gage above Lake Mendocino (11461500; Figure 11a) and the downstream-most gage (11467000), which is influenced by reservoir operations at Lake Mendocino and Lake Sonoma (Figure 11a). We obtained the naturalized flows at the latter gage by calculating the difference of simulated streamflow with and without a reservoir module at this gage and then adding the difference back to its observations, following Cao et al. (2019). We used the Kling-Gupta efficiency (KGE; Gupta et al., 2009) to evaluate the goodness-of-fit between hourly streamflow observations and hourly simulations at these two gages. KGE facilitates analysis of the various statistical components of the Nash-Sutcliffe efficiency, which is an objective method to evaluate runoff performance in hydrologic models.

6.2. Modeling Results

Soil moisture observations can provide information for situational awareness and model initialization on antecedent wetness conditions of a basin, a critical factor for flood forecasting (e.g., Brocca et al., 2010; Leroux et al., 2016; Zhang et al., 2016) as well as landslide forecasting (e.g., Godt et al., 2006; Thomas et al., 2018). Results showed that the KGE during the storm (0800 UTC 13 February 2019 to 0800 UTC 16 February 2019) increased from 0.19 to 0.42 by updating the surface layer, from 0.19 to 0.54 by updating the top two layers, and 0.19 to 0.66 by updating all three layers at the upstream USGS gage 11461500 (Figure 11d). This heavily instrumented gage is surrounded by 7 out of 12 HMT sites in the Russian River watershed. Improvements increased as observations from deeper depths were included. However, the KGE at the downstream-most USGS gage 1146700 did not increase with each additional depth (Figure 11e). The KGE changed from 0.89 to 0.95, 0.90, and 0.70, respectively, with updates of the uppermost layer only, upper two layers, and all three layers. This result is possibly due to the sparse distribution of the downstream HMT sites (Figure 11a) and the influence of historical calibration at different stream gage locations. Although these results are for a single storm, they do have implications for placement of soil moisture stations and for the manner in which the updating is performed. These results suggest that flood forecasting is likely to benefit from both measurements at depths beyond the surface layer and a denser spatial distribution of soil moisture observations in the drainage area of interest. These measurements also support landslide hazard monitoring (Thomas et al., 2019).

7. Discussion

ARs drive extreme hydrometeorological events and hydroclimate variability worldwide (Paltan et al., 2017). Impacts from ARs, especially in California, are expected to increase in a warming and increasingly variable climate (Gershunov et al., 2019). Data provided by California's multitiered observational network facilitate development of conceptual linkages between natural hazards and meteorological or hydrological precursor and triggering conditions during ARs. With respect to forecasting and from an event-based perspective, we find that:

1. Linkages are deepened by incorporating additional observational networks, such as the GNSS/GPS network and ALERT gauges (section 4) or seismic networks (section 5.3).
2. Regionally specific information advances a comprehensive perspective of the event.

3. Aircraft-based observations provided unique perspectives regarding the structure and intensity of the AR offshore (section 3).
4. Assimilation of targeted offshore data into numerical weather prediction models in otherwise data-sparse regions (e.g., the North Pacific) demonstrates promise for improving forecast skill (Demirdjian et al., 2020; Stone et al., 2020).
5. Incorporation of model products, such as VIC soil moisture percentiles, provides useful information for anticipating impacts from forecast events.
6. Soil moisture before and following the event (Figures 2b–2c and 5) indicates when steepland regions are likely to produce runoff if additional precipitation occurs.
7. Soil moisture conditions following the Valentine's Day storm suggest continued widespread natural hazard risks from flooding (Cao et al., 2019), mass wasting (Oakley, Lancaster, et al., 2018), and degraded coastal water quality (Aguilera et al., 2019).
8. Soil moisture observations improved hydrologic model flood forecasts (section 6).

The present study, as well as other work utilizing data from the network (e.g., Martin et al., 2018; Ralph et al., 2013; Sterle et al., 2019; Sumargo et al., 2020; Wang et al., 2019; White et al., 2019), indicates the network is capable of achieving the goals outlined in Ralph et al. (2014) and White et al. (2013). These goals include the following:

1. Improved understanding of physical processes, model limitations, and climate trend analysis (Ralph et al., 2014).
2. Direct characterizations of extreme events and how they can inform resource and hazards management.

The high temporal resolution of the network and diverse data sources (e.g., models, aircraft, and in situ) documents and provides deeper understanding of various event outcomes that otherwise may be missed. Examples include the following:

1. Verifying the record precipitable water in southern California (section 4).
2. Reporting the dramatic oscillations in snow level in northern California and the Sierra Nevada (section 5.1).
3. Constraining the timing of the Mt. Shasta avalanche (section 5.3).

Knowledge of these outcomes can be leveraged to identify weaknesses in numerical model output, such as CNRFC freezing level forecasts (section 5.1). Given how warm the Valentine's Day storm was, errors in model freezing levels are expected to be larger than normal circumstances (Henn et al., 2020). The magnitudes of snow level oscillations, which nearly spanned the range of historic observations (Figure 8), provide a scenario for model experiments aimed at improving snow level forecast skill.

In challenging forecast scenarios, such as low or variable snow levels (sections 5.1–5.2), model validation is performed in real-time at coastal AROs (Figure S5) and at snow level radar sites (Figure S6; Ray & White, 2019). AROs combine numerous observations with short-term high-resolution model simulations to enhance short-term forecasting for these situations. This "Integrated Water Vapor Flux Tool" (Neiman et al., 2009; Figure S5) was first used in conjunction with rapidly updating forecast models (White et al., 2012), but now exists with multiple operational and research versions of weather models (e.g., Cordeira et al., 2017; Ray & White, 2019). The water vapor flux tool provides a recent history of key parameters associated with observed AR-related features such as upslope water vapor flux, precipitation, and recent model forecast performance. This information can influence forecaster confidence regarding the next 12-hr forecast period and impact-based decision support (Uccellini & Ten Hoeve, 2019) on issuing or extending weather-related warnings based on whether or not heavy precipitation is forecast to continue. We recommend model forecasts and recent verification statistics be expanded to all suites of instruments, such as the GNSS/GPS sensors and snow pillows, especially as modeling capabilities move toward ensemble-based, probabilistic forecasts (e.g., National Blend of Models; Hamill et al., 2017). Discovering model weaknesses in reproducing observed phenomena, such as freezing level variability (Henn et al., 2020), motivates targeted improvements in forecast skill (e.g., Olson et al., 2019). These improvements can enhance public and emergency management preparedness and response during, and following, extreme events.

The importance of snow and freezing level oscillations (section 5.1) in operational runoff forecasts is an example of how improved forecasts and process-based understanding can benefit water management.

This is a key aim of the multitiered observational network (Ralph et al., 2014; White et al., 2013). Snow level variability at the mountain range scale means the water conveyance system should be managed between different operator groups to ensure reservoir releases can be made with minimal downstream flood impacts while keeping within reservoir operational constraints (White et al., 2010). Our analysis of the impact of the snow level oscillations and streamflow responses in the northern Sierra Nevada (Figure 8) is limited by the daily resolution of upstream reservoir storage data along the Middle Fork of the American River. To overcome these challenges of reservoir management in snow-dominated watersheds, we note that:

1. Sub-daily reservoir storage data are needed to address whether streamflow responses are natural or the result of reservoir operations.
2. Sub-daily observations of soil moisture, precipitation, and streamflow on both impaired and unimpaired river basins are needed to evaluate physical drivers of hydrologic responses and facilitate calibrating models aimed at reproducing these responses (section 6).
3. High-resolution soil moisture and precipitation observations in complex terrain would improve the ability to provide landslide early warnings.

The increasing exposure of life and property to natural hazards amidst climate change and population growth virtually demands integrated observational networks to support long-term management goals (Lundquist et al., 2016). Improving the real-time accessibility of observational data from the kinds of diverse networks explored here is a necessary step if these data are to be used to meet goals of achieving water supply reliability, flood risk management, and the understanding of and resiliency to other extreme events (e.g., mass movement, wildfire, and heat extremes). These networks contribute toward improved understanding of current hydroclimate conditions, predictions of how different environments will respond to extreme events under various antecedent conditions, and assessments of forecast performance. The complexity of natural systems presents a challenge for quickly characterizing the range of possible outcomes from a given extreme event. In the case of California's network, many of these observations have been collected over varied antecedent conditions in the past decade. This allows events to be placed into the context of past extreme climate conditions over longer timescales (e.g., Hatchett et al., 2018; Sterle et al., 2019). Additional confidence in understanding potential outcomes allows focused efforts on mitigating impacts, a key goal of decision support (Uccellini & Ten Hoeve, 2019).

8. Concluding Remarks

California's multitiered network of diverse observations provides real-time information pertinent to the analysis of extreme events. These observations help characterize triggering mechanisms and impacts for a variety of natural hazards, and thus can make natural hazard risk mitigation more achievable through improvements in forecasting and decision support aimed at timely resource positioning. Our goal was to explore and illustrate the utility of California's uniquely diverse collection of networks by exploring the physical origins of impacts during the 2019 Valentine's Day winter storm. We conclude that California's observational network is successfully implementing ideas that emerged from multiagency planning efforts (summarized in Ralph et al., 2014, and White et al., 2013) and of testing and demonstration carried out through the NOAA Hydrometeorology Testbed (Ralph et al., 2013; White et al., 2012).

Components of the network with many years of observations, such as snow level radar, soil moisture, and GPS water vapor, can now be used to place extreme events into climatological context and establish the baseline for regional hydroclimate conditions (e.g., Cao et al., 2019; Hatchett, Daudert, et al., 2017; Sterle et al., 2019). By helping identify drivers of hydrometeorological impacts in sensitive ecosystems or to values-at-risk, the network can provide a basis for prioritizing future investments and studies aimed at mitigating risks and enhancing the reliability of local and regional water resources (Ralph et al., 2014; White et al., 2013). Further investments in maintaining and enhancing these observational networks will be necessary in a changing world (e.g., Lundquist et al., 2016; Mensing et al., 2013). Process-based understanding and subsequent improvements in forecast confidence at longer lead times will translate into better decision support during events and can inform longer-term shifts to the water management landscape. California's networks provide a basis for continually improving early warning and emergency response times during events like the 2019 Valentine's Day storm by providing up-to-date and actionable information.

References

Abatzoglou, J. T. (2013). Development of gridded surface meteorological data for ecological applications and modelling. *International Journal of Climatology*, *33*(1), 121–131. https://doi.org/10.1002/joc.3413

Abatzoglou, J. T., & Magnusdottir, G. (2006). Planetary wave breaking and nonlinear reflection: Seasonal cycle and interannual variability. *Journal of Climate*, *19*(23), 6139–6152. https://doi.org/10.1175/JCLI3968.1

Aguilera, R., Gershunov, A., & Benmarhnia, T. (2019). Atmospheric rivers impact California's coastal water quality via extreme precipitation. *Science of the Total Environment*, *671*, 488–494. https://doi.org/10.1016/j.scitotenv.2019.03.318

Bedsworth, L., Cayan, D., Franco, G., Fisher, L., & Sonya Ziaja. (2018). California's Fourth Climate Change Assessment: Statewide Summary Report, SUM-CCCA4–2018-013, available at: [https://www.energy.ca.gov/sites/default/files/2019-11/Statewide_Reports-SUM-CCCA4-2018-013_Statewide_Summary_Report_ADA.pdf

Bevis, M., Businger, S., Herring, T. A., Rocken, C., Anthes, R. A., & Ware, R. H. (1992). GPS meteorology: Remote sensing of atmospheric water vapor using the Global Positioning System. *Journal of Geophysical Research*, *97*(D14), 15,787–15,801. https://doi.org/10.1029/92JD01517

Bohn, T. J., Livneh, B., Oyler, J. W., Running, S. W., Nijssen, B., & Lettenmaier, D. P. (2013). Global evaluation of MTCLIM and related algorithms for forcing of ecological and hydrological models. *Agricultural and Forest Meteorology*, *176*, 38–49. https://doi.org/10.1016/j.agrformet.2013.03.003

Brocca, L., Melone, F., Moramarco, T., Wagner, W., Naeimi, V., Bartalis, Z., & Hasenauer, S. (2010). Improving runoff prediction through the assimilation of the ASCAT soil moisture product. *Hydrology and Earth System Sciences*, *14*(10), 1881–1893. https://doi.org/10.5194/hess-14-1881-2010

Burgess, W. P., Beard, R. A., Lancaster, J. T., & Wurgler, R. A. (2019). California recent reported landslide map. [Available at: http://maps.conservation.ca.gov/cgs/lsi/app/]

California Department of Transportation (Caltrans). (2019). Public records request: R003575–082019.

Cannon, S. H., Gartner, J. E., Wilson, R. C., Bowers, J. C., & Laber, J. L. (2008). Storm rainfall conditions for floods and debris flows from recently burned areas in southwestern Colorado and southern California. *Geomorphology*, *96*(3–4), 250–269. https://doi.org/10.1016/j.geomorph.2007.03.019

Cao, Q., Mehran, A., Ralph, F. M., & Lettenmaier, D. P. (2019). The Role of Hydrological Initial Conditions on Atmospheric River Floods in the Russian River Basin. *Journal of Hydrometeorology*, *20*, 1667–1686. https://doi.org/10.1175/JHM-D-19-0030.1

Cayan, D. R., Dettinger, M. D., Pierce, D., Das, T., Knowles, N., Ralph, F. M., & Sumargo, E. (2016). Natural variability, anthropogenic climate change, and impacts on water availability and flood extremes in the Western United States. *Water Policy and Planning in a Variable and Changing Climate* (Vol. 2, pp. 17–44). Boca Raton, FL: CRC Press. https://doi.org/10.1201/b19534-4

Cifelli, R., Chandrasekar, V., Chen, H., & Johnson, L. E. (2018). High resolution radar quantitative precipitation estimation in the San Francisco Bay area: Rainfall monitoring for the urban environment. *Journal of the Meteorological Society of Japan Series II*, *96A*, 141–155. https://doi.org/10.2151/jmsj.2018-016

Collins, B. D., & Corbett, S. C. (2019). Terrestrial lidar data of the February 14, 2019 Sausalito Boulevard Landslide, Sausalito, California. *U. S. Geological Survey Data Series 1112*, 1–12. https://doi.org/10.3133/ds1112

Cordeira, J. M., Ralph, F. M., Martin, A., Gaggini, N., Spackman, J. R., Neiman, P. J., et al. (2017). Forecasting atmospheric rivers during CalWater 2015. *Bulletin of the American Meteorological Society*, *98*(3), 449–459. https://doi.org/10.1175/BAMS-D-15-00245.1

Corringham, T. W., Ralph, F. M., Gershunov, A., Cayan, D. R., & Talbot, C. A. (2019). Atmospheric rivers drive flood damages in the western United States. *Science Advances*, *5*, eaax4631. https://doi.org/10.1126/sciadv.aax4631

Demirdjian, R., Norris, J. R., Martin, A., & Ralph, F. M. (2020). Dropsonde observations of the ageostrophy within the pre-cold-frontal low-level jet associated with atmospheric rivers. *Monthly Weather Review*, *148*, 1389–1406. https://doi.org/10.1175/MWR-D-19-0248.1

Dettinger, M. D., Ralph, F. M., Das, T., Neiman, P. J., & Cayan, D. R. (2011). Atmospheric rivers, floods and the water resources of California. *Water*, *3*(2), 445–478. https://doi.org/10.3390/w3020445

NOAA Environmental Modeling Center. (2003). The GFS atmospheric model. NOAA/NCEP/Environmental Modeling Center Office Note 442, 14 pp. [Available at http://www.emc.ncep.noaa.gov/officenotes/FullTOC.html].

Gaspari, G., & Cohn, S. E. (1999). Construction of correlation functions in two and three dimensions. *Quarterly Journal of the Royal Meteorological Society*, *125*(554), 723–757. https://doi.org/10.1002/qj.49712555417

Gelaro, R., McCarty, W., Suárez, M. J., Todling, R., Molod, A., Takacs, L., et al. (2017). The modern-era retrospective analysis for research and applications, version 2 (MERRA-2). *Journal of Climate*, *30*(14), 5419–5454. https://doi.org/10.1175/JCLI-D-16-0758.1

Gershunov, A., Shulgina, T., Clemesha, R. E., Guirguis, K., Pierce, D. W., Dettinger, M. D., et al. (2019). Precipitation regime change in Western North America: The role of atmospheric rivers. *Scientific Reports*, *9*, 9944. https://doi.org/10.1038/s41598-019-46169-w

Godt, J. W., Baum, R. L., & Chleborad, A. F. (2006). Rainfall characteristics for shallow landsliding in Seattle, Washington, USA. *Earth Surface Processes Landforms*, *31*, 97–110. https://doi.org/10.1002/esp.1237

Gupta, H. V., Kling, H., Yilmaz, K. K., & Martinez, G. F. (2009). Decomposition of the mean squared error and NSE performance criteria: Implications for improving hydrological modelling. *Journal of Hydrology*, *377*(1–2), 80–91. https://doi.org/10.1016/j.jhydrol.2009.08.003

Hamill, T. M., Engle, E., Myrick, D., Peroutka, M., Finan, C., & Scheuerer, M. (2017). The US National Blend of Models for statistical postprocessing of probability of precipitation and deterministic precipitation amount. *Monthly Weather Review*, *145*(9), 3441–3463. https://doi.org/10.1175/MWR-D-16-0331.1

Hansen, C., & Underwood, S. J. (2012). Synoptic scale weather patterns and size-5 avalanches on Mt. Shasta, California. *Northwest Science*, *86*(4), 329–341. https://doi.org/10.3955/046.086.0408

Hatchett, B. (2018). Snow level characteristics and impacts of a spring typhoon-originating atmospheric river in the Sierra Nevada, USA. *Atmosphere*, *9*(6), 233. https://doi.org/10.3390/atmos9060233

Hatchett, B., Daudert, B., Garner, C., Oakley, N., Putnam, A., & White, A. (2017). Winter snow level rise in the northern Sierra Nevada from 2008 to 2017. *Water*, *9*, 899. https://doi.org/10.3390/w9110899

Hatchett, B. J., Boyle, D. P., Garner, C. B., Kaplan, M. L., Bassett, S. D., & Putnam, A. E. (2018). Sensitivity of a western Great Basin terminal lake to winter northeast Pacific storm track activity and moisture transport. *Geological Society of America Special Papers*, *536*, 67–79. https://doi.org/10.1130/2018.2536(05

Hatchett, B. J., Burak, S., Rutz, J. J., Oakley, N. S., Bair, E. H., & Kaplan, M. L. (2017). Avalanche fatalities during atmospheric river events in the western United States. *Journal of Hydrometeorology*, *18*(5), 1359–1374. https://doi.org/10.1175/JHM-D-16-0219.1

Hatchett, B. J., Kaplan, M. L., & Burak, S. (2016). Some characteristics of upside-down storms in the northern Sierra Nevada, California-Nevada, USA. Proceedings of the International Snow Science Workshop, Breckenridge, CO. Available at: [http://arc.lib.montana.edu/snow-science/objects/ISSW16_P4.03.pdf]

Henn, B., Weihs, R., Martin, A. C., Ralph, F. M., & Osborne, T. (2020). Skill of rain–snow level forecasts for landfalling atmospheric rivers: A multimodel assessment using California's network of vertically profiling radars. *Journal of Hydrometeorology*, *21*(4), 751–771. https://doi.org/10.1175/JHM-D-18-0212.1

Hu, H., Dominguez, F., Wang, Z., Lavers, D. A., Zhang, G., & Ralph, F. M. (2017). Linking atmospheric river hydrological impacts on the US West Coast to Rossby wave breaking. *Journal of Climate*, *30*(9), 3381–3399. https://doi.org/10.1175/JCLI-D-16-0386.1

Johnston, P. E., Jordan, J. R., White, A. B., Carter, D. A., Costa, D. M., & Ayers, T. E. (2017). The NOAA FM-CW snow-level radar. *Journal of Atmospheric and Oceanic Technology*, *34*(2), 249–267. https://doi.org/10.1175/JTECH-D-16-0063.1

Kishimura, K., & Izumi, K. (1997). Seismic signals induced by snow avalanche flow. *Natural Hazards*, *15*(1), 89–100. https://doi.org/10.1023/A:1007934815584

Lamjiri, M. A., Dettinger, M. D., Ralph, F. M., & Guan, B. (2017). Hourly storm characteristics along the US West Coast: Role of atmospheric rivers in extreme precipitation. *Geophysical Research Letters*, *44*, 7020–7028. https://doi.org/10.1002/2017GL074193

Lamjiri, M. A., Ralph, F. M., & Dettinger, M. D. (2020). Recent changes in United States extreme 3-day precipitation using the R-CAT scale. *Journal of Hydrometeorology*, *21*(6), 1207–1221. https://doi.org/10.1175/JHM-D-19-0171.1

Lavers, D. A., Waliser, D. E., Ralph, F. M., & Dettinger, M. D. (2016). Predictability of horizontal water vapor transport relative to precipitation: Enhancing situational awareness for forecasting western U.S. extreme precipitation and flooding. *Geophysical Research Letters*, *43*, 2275–2282. https://doi.org/10.1002/2016GL067765

Leroux, D. J., Pellarin, T., Vischel, T., Cohard, J. M., Gascon, T., Gibon, F., et al. (2016). Assimilation of SMOS soil moisture into a distributed hydrological model and impacts on the water cycle variables over the Ouémé catchment in Benin. *Hydrology and Earth System Sciences*, *20*(7), 2827–2840. https://doi.org/10.5194/hess-20-2827-2016

Liang, X., Lettenmaier, D. P., Wood, E. F., & Burges, S. J. (1994). A simple hydrologically based model of land surface water and energy fluxes for general circulation models. *Journal of Geophysical Research*, *99*(D7), 14,415–14,428. https://doi.org/10.1029/94JD00483

Liu, Q. H., & Weng, F. Z. (2005). One-dimensional variational retrieval algorithm of temperature, water vapor, and cloud water profiles from advanced microwave sounding unit (AMSU). *IEEE Transactions on Geoscience and Remote Sensing*, *43*(5), 1087–1095. https://doi.org/10.1109/TGRS.2004.843211

Lundquist, J. D., & Cayan, D. R. (2007). Surface temperature patterns in complex terrain: Daily variations and long-term change in the central Sierra Nevada, California. *Journal of Geophysical Research*, *112*, D11124. https://doi.org/10.1029/2006JD007561

Lundquist, J. D., Neiman, P. J., Martner, B., White, A. B., Gottas, D. J., & Ralph, F. M. (2008). Rain versus snow in the Sierra Nevada, California: Comparing Doppler profiling radar and surface observations of melting level. *Journal of Hydrometeorology*, *9*(2), 194–211. https://doi.org/10.1175/2007JHM853.1

Lundquist, J. D., Roche, J. W., Forrester, H., Moore, C., Keenan, E., Perry, G., et al. (2016). Yosemite Hydroclimate Network: Distributed stream and atmospheric data for the Tuolumne River watershed and surroundings. *Water Resources Research*, *52*, 7478–7489. https://doi.org/10.1002/2016WR019261

Mao, Y., Nijssen, B., & Lettenmaier, D. P. (2015). Is climate change implicated in the 2013–2014 California drought? A hydrologic perspective. *Geophysical Research Letters*, *42*, 2805–2813. https://doi.org/10.1002/2015GL063456

Martin, A., Ralph, F. M., Demirdjian, R., DeHaan, L., Weihs, R., Helly, J., et al. (2018). Evaluation of atmospheric river predictions by the WRF model using aircraft and regional mesonet observations of orographic precipitation and its forcing. *Journal of Hydrometeorology*, *19*(7), 1097–1113. https://doi.org/10.1175/JHM-D-17-0098.1

Mensing, S., Strachan, S., Arnone, J., Fenstermaker, L., Biondi, F., Devitt, D., et al. (2013). A network for observing Great Basin climate change. *Eos, Transactions American Geophysical Union*, *94*(11), 105–106. https://doi.org/10.1002/2013EO110001

Minder, J. R., Durran, D. R., & Roe, G. H. (2011). Mesoscale controls on the mountainside snow line. *Journal of the Atmospheric Sciences*, *68*(9), 2107–2127. https://doi.org/10.1175/JAS-D-10-05006.1

Minder, J. R., & Kingsmill, D. E. (2013). Mesoscale variations of the atmospheric snow line over the northern Sierra Nevada: Multiyear statistics, case study, and mechanisms. *Journal of the Atmospheric Sciences*, *70*(3), 916–938. https://doi.org/10.1175/JAS-D-12-0194.1

Moore, A. W., Small, I. J., Gutman, S. I., Bock, Y., Dumas, J. L., Fang, P., et al. (2015). National Weather Service Forecasters use GPS precipitable water vapor for enhanced situational awareness during the Southern California summer monsoon. *Bulletin of the American Meteorological Society*, *96*(11), 1867–1877. https://doi.org/10.1175/BAMS-D-14-00095.1

Moore, B. J., Keyser, D., & Bosart, L. F. (2019). Linkages between extreme precipitation events in the central and eastern United States and Rossby wave breaking. *Monthly Weather Review*, *147*(9), 3327–3349. https://doi.org/10.1175/MWR-D-19-0047.1

Morrison, I., & Businger, S. (2001). Synoptic structure and evolution of a Kona low. *Weather and Forecasting*, *16*(1), 81–98. https://doi.org/10.1175/1520-0434(2001)016<0081:SSAEOA>2.0.CO;2

Mount Shasta Avalanche Center. (2019). Mount Shasta Avalanche and Climbing Information. . https://www.shastaavalanche.org/

Nardi, K. M., Barnes, E. A., & Ralph, F. M. (2018). Assessment of numerical weather prediction model reforecasts of the occurrence, intensity, and location of atmospheric rivers along the West Coast of North America. *Monthly Weather Review*, *146*(10), 3343–3362. https://doi.org/10.1175/MWR-D-18-0060.1

Neiman, P. J., Hughes, M., Moore, B. J., Ralph, F. M., & Sukovich, E. M. (2013). Sierra barrier jets, atmospheric rivers, and precipitation characteristics in Northern California: A composite perspective based on a network of wind profilers. *Monthly Weather Review*, *141*(12), 4211–4233. https://doi.org/10.1175/MWR-D-13-00112.1

Neiman, P. J., White, A. B., Ralph, F. M., Gottas, D. J., & Gutman, S. I. (2009). A water vapour flux tool for precipitation forecasting. *Proceedings of the Institution of Civil Engineers: Water Management*, *162*(2), 83–94. https://doi.org/10.1680/wama.2009.162.2.83

Northern California Earthquake Data Center (NCEDC) (2014). Northern California Earthquake Data Center. UC Berkeley Seismological Laboratory. Dataset. https://doi.org/10.7932/NCEDC

Oakley, N. S., Cannon, F., Munroe, R., Lancaster, J. T., Gomberg, D., & Ralph, F. M. (2018). Brief communication: Meteorological and climatological conditions associated with the 9 January 2018 post-fire debris flows in Montecito and Carpinteria, California, USA. *Natural Hazards and Earth System Sciences*, *18*(11), 3037–3043. https://doi.org/10.5194/nhess-18-3037-2018

Oakley, N. S., Lancaster, J. T., Hatchett, B. J., Stock, J., Ralph, F. M., Roj, S., & Lukashov, S. (2018). A 22-year climatology of cool season hourly precipitation thresholds conducive to shallow landslides in California. *Earth Interactions*, *22*(14), 1–35. https://doi.org/10.1175/EI-D-17-0029.1

Oakley, N. S., Lancaster, J. T., Kaplan, M. L., & Ralph, F. M. (2017). Synoptic conditions associated with cool season post-fire debris flows in the Transverse Ranges of southern California. *Natural Hazards*, *88*(1), 327–354. https://doi.org/10.1007/s11069-017-2867-6

Olson, J. B., Kenyon, J. S., Djalalova, I., Bianco, L., Turner, D. D., Pichugina, Y., et al. (2019). Improving wind energy forecasting through numerical weather prediction model development. *Bulletin of the American Meteorological Society*, *100*(11), 2201–2220. https://doi.org/10.1175/BAMS-D-18-0040.1

Paltan, H., Waliser, D., Lim, W. H., Guan, B., Yamazaki, D., Pant, R., & Dadson, S. (2017). Global floods and water availability driven by atmospheric rivers. *Geophysical Research Letters*, *44*, 10,387–10,395. https://doi.org/10.1002/2017GL074882

Parish, T. (1982). Barrier winds along the Sierra Nevada mountains. *Journal of Applied Meteorology*, *12*, 925–930. https://doi.org/10.1175/1520-0450(1982)021<0925:BWATSN>

Payne, A. E., & Magnusdottir, G. (2014). Dynamics of landfalling atmospheric rivers over the North Pacific in 30 years of MERRA reanalysis. *Journal of Climate*, *27*(18), 7133–7150. https://doi.org/10.1175/JCLI-D-14-00034.1

Prowse, T. D., & Owens, I. F. (1984). Characteristics of snowfalls, snow metamorphism, and snowpack structure with implications for avalanching, Craigieburn Range, New Zealand. *Arctic and Alpine Research*, *16*(1), 107–118. https://doi.org/10.2307/1551176

Ralph, F. M., Cannon, F., Tallapragada, V., Davis, C. A., Doyle, J. D., Pappenberger, F., et al. (2020). West Coast forecast challenges and development of atmospheric river reconnaissance. *Bulletin of the American Meteorological Society*. https://doi.org/10.1175/BAMS-D-19-0183.1

Ralph, F. M., Cordeira, J. M., Neiman, P. J., & Hughes, M. (2016). Landfalling atmospheric rivers, the Sierra barrier jet, and extreme daily precipitation in Northern California's Upper Sacramento River watershed. *Journal of Hydrometeorology*, *17*(7), 1905–1914. https://doi.org/10.1175/JHM-D-15-0167.1

Ralph, F. M., Dettinger, M., White, A., Reynolds, D., Cayan, D., Schneider, T., et al. (2014). A vision for future observations for western US extreme precipitation and flooding. *Journal of Contemporary Water Research & Education*, *153*(1), 16–32. https://doi.org/10.1111/j.1936-704X.2014.03176.x

Ralph, F. M., & Dettinger, M. D. (2012). Historical and National Perspectives on extreme West Coast precipitation associated with atmospheric rivers during December 2010. *Bulletin of the American Meteorological Society*, *93*(6), 783–790. https://doi.org/10.1175/BAMS-D-11-00188.1

Ralph, F. M., Intrieri, J., Andra, D. Jr., Atlas, R., Boukabara, S., Bright, D., et al. (2013). The emergence of weather-related test beds linking research and forecasting operations. *Bulletin of the American Meteorological Society*, *94*(8), 1187–1211. https://doi.org/10.1175/BAMS-D-12-00080.1

Ralph, F. M., Neiman, P. J., Wick, G. A., Gutman, S. I., Dettinger, M. D., Cayan, D. R., & White, A. B. (2006). Flooding on California's Russian River: Role of atmospheric rivers. *Geophysical Research Letters*, *33*, L13801. https://doi.org/10.1029/2006GL026689

Ralph, F. M., Rutz, J. J., Cordeira, J. M., Dettinger, M., Anderson, M., Reynolds, D., et al. (2019). A scale to characterize the strength and impacts of atmospheric rivers. *Bulletin of the American Meteorological Society*, *100*(2), 269–289. https://doi.org/10.1175/BAMS-D-18-0023.1

Ray, A. J., & White, A. B. (2019). The hydrometeorology testbed–west legacy observing network: Supporting research to applications for atmospheric rivers and beyond. *Atmosphere*, *10*, 533. https://doi.org/10.3390/atmos10090533

Roberts, M. T. (2019). *Mesoscale Controls on the Shasta County Convergence Zone* (1–105). M.S. Thesis, San José State University. https://scholarworks.sjsu.edu/etd_theses/5043

Rondanelli, R., Hatchett, B., Rutllant, J., Bozkurt, D., & Garreaud, R. (2019). Strongest MJO on record triggers extreme Atacama rainfall and warmth in Antarctica. *Geophysical Research Letters*, *46*, 3482–3491. https://doi.org/10.1029/2018GL081475

Rutz, J. J., Steenburgh, W. J., & Ralph, F. M. (2014). Climatological characteristics of atmospheric rivers and their inland penetration over the western United States. *Monthly Weather Review*, *142*(2), 905–921. https://doi.org/10.1175/MWR-D-13-00168.1

Staley, D. M., Negri, J. A., Kean, J. W., Laber, J. L., Tillery, A. C., & Youberg, A. M. (2017). Prediction of spatially explicit rainfall intensity–duration thresholds for post-fire debris-flow generation in the western United States. *Geomorphology*, *278*, 149–162. https://doi.org/10.1016/j.geomorph.2016.10.019

Sterle, K., Hatchett, B. J., Singletary, L., & Pohll, G. (2019). Hydroclimate variability in snow-fed river systems: Local water managers' perspectives on adapting to the new normal. *Bulletin of the American Meteorological Society*, *100*(6), 1031–1048. https://doi.org/10.1175/BAMS-D-18-0031.1

Stone, R. E., Reynolds, C. A., Doyle, J. D., Langland, R., Baker, N., Lavers, D. A., & Ralph, F. M. (2020). Atmospheric river reconnaissance observation impact in the navy global forecast system. *Monthly Weather Review*, *148*(2), 763–782. https://doi.org/10.1175/MWR-D-19-0101.1

Sumargo, E., Wilson, A. M., Ralph, F. M., Weihs, R., White, A., Jasperse, J., et al. (2020). The hydrometeorological observation network in California's Russian River watershed: Development, characteristics and key findings from 1997 to 2019. *Bulletin of the American Meteorological Society*. https://doi.org/10.1175/BAMS-D-19-0253.1

Desert Sun. (2019). Palm Springs declares local emergency after flooding causes nearly $1.9 million in damage. Available at: [https://www.desertsun.com/story/news/local/palm-springs/2019/03/07/palm-springs-declares-emergency-outlines-nearly-2-million-flood-damage/3087113002/]

Swain, D. L. (2015). A tale of two California droughts: Lessons amidst record warmth and dryness in a region of complex physical and human geography. *Geophysical Research Letters*, *42*, 9999–10,003. https://doi.org/10.1002/2015GL066628

Talbot, C.A., Ralph, F. M., & Jasperse, J. (2019). Forecast-informed reservoir operations: Lessons learned from a multi-agency joint research and operations effort. Federal Interagency Sedimentation and Hydrologic Modeling Conference, June 25–28, Reno, Nevada. Available at: [https://www.sedhyd.org/2019/openconf/modules/request.php?module=oc_proceedings&action=view.php&id=320&file=1/320.pdf&a=Accept]

Thomas, M. A., Collins, B. D., & Mirus, B. B. (2019). Assessing the feasibility of satellite-based thresholds for hydrologically driven landsliding. *Water Resources Research*, *55*, 9006–9023. https://doi.org/10.1029/2019WR025577

Thomas, M. A., Mirus, B. B., Collins, B. D., Lu, N., & Godt, J. W. (2018). Variability in soil-water retention properties and implications for physics-based simulation of landslide early warning criteria. *Landslides*, *15*(7), 1265–1277. https://doi.org/10.1007/s10346-018-0950-z

Thorncroft, C. D., Hoskins, B. J., & McIntyre, M. E. (1993). Two paradigms of baroclinic-wave life-cycle behaviour. *Quarterly Journal of the Royal Meteorological Society*, *119*(509), 17–55. https://doi.org/10.1002/qj.49711950903

Uccellini, L. W., & Ten Hoeve, J. E. (2019). Evolving the National Weather Service to build a weather-ready nation: Connecting observations, forecasts, and warnings to decision makers through impact-based decision support services. *Bulletin of the American Meteorological Society*, *100*(10), 1923–1942. https://doi.org/10.1175/BAMS-D-18-0159.1

Underwood, S. J., Kaplan, M. L., & King, K. C. (2009). The role of upstream midtropospheric circulations in the Sierra Nevada enabling leeside (spillover) precipitation. Part I: A synoptic-scale analysis of spillover precipitation and flooding in a leeside basin. *Journal of Hydrometeorology*, *10*(6), 1327–1354. https://doi.org/10.1175/2009JHM1106.1

Vilajosana, I., Khazaradze, G., Surinach, E., Lied, E., & Kristensen, K. (2007). Snow avalanche speed determination using seismic methods. *Cold Regions Science and Technology*, *49*(1), 2–10. https://doi.org/10.1016/j.coldregions.2006.09.007

Wang, M., Wang, J., Bock, Y., Liang, H., Dong, D., & Fang, P. (2019). Dynamic mapping of the movement of landfalling atmospheric rivers over Southern California with GPS data. *Geophysical Research Letters*, *46*, 3551–3559. https://doi.org/10.1029/2018GL081318

White, A. B., Anderson, M. L., Dettinger, M. D., Ralph, F. M., Hinojosa, A., Cayan, D. R., et al. (2013). A twenty-first-century California observing network for monitoring extreme weather events. *Journal of Atmospheric and Oceanic Technology*, *30*(8), 1585–1603. https://doi.org/10.1175/JTECH-D-12-00217.1

White, A. B., Colman, B., Carter, G. M., Ralph, F. M., Webb, R. S., Brandon, D. G., et al. (2012). NOAA's rapid response to the Howard A. Hanson Dam flood risk management crisis. *Bulletin of the American Meteorological Society*, *93*(2), 189–207. https://doi.org/10.1175/Bams-D-11-00103.1

White, A. B., Gottas, D. J., Henkel, A. F., Neiman, P. J., Ralph, F. M., & Gutman, S. I. (2010). Developing a performance measure for snow-level forecasts. *Journal of Hydrometeorology*, *11*(3), 739–753. https://doi.org/10.1175/2009JHM1181.1

White, A. B., Moore, B. J., Gottas, D. J., & Neiman, P. J. (2019). Winter storm conditions leading to excessive runoff above California's Oroville Dam during January and February 2017. *Bulletin of the American Meteorological Society*, *100*(1), 55–70. https://doi.org/10.1175/BAMS-D-18-0091.1

White, A. B., Ralph, F. M., Neiman, P. J., Gottas, D. J., & Gutman, S. I. (2009). The NOAA coastal atmospheric river observatory. Paper presented at the *34th Conference on Radar Meteorology*, American Meteorological Society, Williamsburg, VA.

Wigmosta, M. S., Vail, L. W., & Lettenmaier, D. P. (1994). A distributed hydrology-vegetation model for complex terrain. *Water Resources Research*, *30*(6), 1665–1679. https://doi.org/10.1029/94WR00436

Wimmers, A. J., & Velden, C. S. (2010). Objectively determining the rotational center of tropical cyclones in passive microwave satellite imagery. *Journal of Applied Meteorology and Climatology*, *49*(9), 2013–2034. https://doi.org/10.1175/2010JAMC2490.1

Xiao, M., Koppa, A., Mekonnen, Z., Pagán, B. R., Zhan, S., Cao, Q., et al. (2017). How much groundwater did California's Central Valley lose during the 2012–2016 drought? *Geophysical Research Letters*, *44*, 4872–4879. https://doi.org/10.1002/2017GL073333

Zhang, D., Madsen, H., Ridler, M. E., Kidmose, J., Jensen, K. H., & Refsgaard, J. C. (2016). Multivariate hydrological data assimilation of soil moisture and groundwater head. *Hydrology and Earth System Sciences*, *20*(10), 4341–4357. https://doi.org/10.5194/hess-20-4341-2016